Terahertz spectroscopy of semiconductors and their interfaces

Marco Ballabio

ISBN 978-3-949783-00-5

Marco Ballabio

Terahertz spectroscopy of semiconductors and their interfaces

Terahertz spectroscopy of semiconductors and their interfaces

Terahertz spectroscopy of semiconductors and their interfaces

ACADEMISCH PROEFSCHRIFT

ter verkrijging van de graad van doctor
aan de Universiteit van Amsterdam
op gezag van de Rector Magnificus
prof. dr. ir. K.I.J. Maex
ten overstaan van een door het College voor Promoties ingestelde commissie,
in het openbaar te verdedigen in de Agnietenkapel
op woensdag 24 november 2021, te 13.00 uur

door Marco Ballabio
geboren te Giussano

Promotiecommissie

Promotor:	prof. dr. M. Bonn	Universiteit van Amsterdam
Copromotor:	dr. E. Cánovas Díaz	IMDEA Nanociencia
Overige leden:	prof. dr. A.F. Koenderink	Universiteit van Amsterdam
	dr. A. de Visser	Universiteit van Amsterdam
	prof. dr. M.S. Golden	Universiteit van Amsterdam
	prof. dr. L.D.A. Siebbeles	Technische Universiteit Delft
	prof. dr. X. Feng	Technische Universität Dresden

Faculteit der Natuurwetenschappen, Wiskunde en Informatica

This thesis is dedicated to the memory of my dear friend Eduard Unger.

The work described in this thesis has been performed at the *Max-Planck-Institut für Polymerforschung* (MPIP)
Ackermannweg 10, 55128 Mainz, Germany.

ISBN 978-3-949783-00-5

PUBLICATIONS COVERED IN THIS THESIS

M. Ballabio, D. Fuertes Marrón, N. Barreau, M. Bonn, E. Cánovas, *Composition-Dependent Passivation Efficiency at the CdS/CuIn1-xGaxSe2 Interface.* Advanced Materials 32, **2020**.

M. Ballabio, T. Zhang, C. Chen, P. Zhang, Z. Liao, M. Hambsch, S. Mannsfeld, E. Zschech, H. Sirringhaus, X. Feng, M. Bonn, R. Dong and E. Cánovas, *Band-like Charge Transport in Phytic Acid-Doped Polyaniline Thin Films.* Advanced Functional Materials, **2021**.

OTHER PUBLICATIONS

R. Dong, P. Han, Arora H., M. Ballabio et al. *High-mobility band-like charge transport in a semiconducting two-dimensional metal–organic framework.* Nature Materials 17, 1027–1032, **2018**.

C. Yang, R. Dong, M. Wang et al. *A semiconducting layered metal-organic framework magnet.* Nature Communications 10, 3260, **2019**.

M. Wang, M. Ballabio, M. Wang et al. *Unveiling Electronic Properties in Metal–Phthalocyanine-Based Pyrazine-Linked Conjugated Two-Dimensional Covalent Organic Frameworks.* Journal of the American Chemical Society 141(42), **2019**.

H. Sahabudeen, H. Qi, M. Ballabio, M. Položij, S. Olthof, R. Shivhare, Y. Jing, S. Park, K. Liu, T. Zhang, J. Ma, B. Rellinghaus, S. Mannsfeld, T. Heine, M. Bonn, E. Cánovas, Z. Zheng, U. Kaiser, R. Dong, X. Feng, *Highly Crystalline and Semiconducting Imine-Based Two-Dimensional Polymers Enabled by Interfacial Synthesis* Angewandte Chemie Int. Ed. 59, 6028, **2020**

Contents

Chapter 1

Introduction

The notion of semiconductor was used for the first time by Alessandro Volta in 1782, referring to materials that could discharge his electrometer, unlike insulators, but not as rapidly as metals do. We have to wait until 1833 before Michael Faraday observed for the first time that the resistance of silver sulfide (AgS) decreased with temperature, in contrast with the dependence observed so far in metals.[1] From this milestone, much progress has been made into understanding this class of material, which carried the technological leap of the XX century. Some revolutionary technologies such as electronic computing, memory storage, signal detection, direct solar energy conversion and efficient light emission just to name a few, became in fact reality thanks to semiconductors.

In this chapter, we introduce the concepts of the electrical conduction of semiconductors, with particular attention to two big subclasses: inorganic, crystalline materials as opposed to organic, soft polymers. We first treat the general picture that can be used to model both the systems and, successively, we provide a separate description of the electronic structure of the two classes.

1.1 Charge transport in semiconductors

The return to equilibrium in a system away from equilibrium is of pivotal interest in physics and its understanding makes the creation of active devices possible. The approach to equilibration can occur through

the transport of a physical quantity such as mass, energy, momentum or charge through a set of available states. In the classical and semiclassical frames, the time evolution of the probability density function f of the quantity in exam can be described by the Boltzmann transport equation

$$\frac{\partial f}{\partial t} + \frac{\boldsymbol{p}}{m} \cdot \nabla_r f + \frac{1}{\hbar} \boldsymbol{F} \cdot \nabla_k f = \left(\frac{\partial f}{\partial t} \right)_{\text{coll}} \tag{1.1}$$

where $\boldsymbol{p}$ is the particle momentum and $\boldsymbol{F}$ denotes the applied force field. It is important to note that:

- $\frac{\boldsymbol{p}}{m} \cdot \nabla_r f$ describes the effect of the concentration gradient;
- $\frac{1}{\hbar} \boldsymbol{F} \cdot \nabla_k f$ is the contribution of the external forces;
- $\left(\frac{\partial f}{\partial t} \right)_{\text{coll}}$ is the collisional term.

The very general equation in (1.1) can be refined to describe charge transport. In our case, we need to simplify the expression within the steady-state approximation, following Liouville's theorem

$$\frac{\partial f}{\partial t} = 0 \tag{1.2}$$

and relaxation time approximation

$$\left(\frac{\partial f}{\partial t} \right)_{\text{coll}} = -\frac{f - f_0}{\tau} \tag{1.3}$$

which is a consequence of the assumption that f relaxes to equilibrium f_0 in a mean time τ in absence of force fields and concentration gradients.

$$f = f_0 - \frac{\tau \boldsymbol{p}}{m} \cdot \nabla_r f - \frac{\tau}{\hbar} \boldsymbol{F} \cdot \nabla_k f$$

If we replace the generic term $\boldsymbol{F}$ with the electric force $-e\boldsymbol{E}$, the transport equation can describe the population of charged particles in a conductor.

If we assume a conductive material immersed in a weak, uniform electric field, the equation turns into

$$f = f_0 - \frac{\tau \boldsymbol{p}}{m} \cdot \nabla_r f + \frac{e\tau}{\hbar} \boldsymbol{E} \cdot \nabla_k f$$

or introducing the energy band $\mathcal{E}$ and the identity $\nabla_k f = \frac{\partial f}{\partial \mathcal{E}} \nabla_k \mathcal{E}$,

$$f = f_0 - \frac{\tau}{\hbar} \nabla_k \mathcal{E} \cdot \left(e \frac{\partial f}{\partial \mathcal{E}} \boldsymbol{E} + \nabla_r f \right) \tag{1.4}$$

Equation (1.4) gives a more explicit form of the non-equilibrium distribution and we can now see it depends on:

- the scattering process $\rightarrow$ τ;
- the momentum-energy relation $\rightarrow$ $\nabla_k \mathcal{E}$;
- the applied forces $\rightarrow$ $e \frac{\partial f}{\partial \mathcal{E}} \boldsymbol{E}$;
- the concentration gradient $\rightarrow$ $\nabla_r f$.

From the same form of the transport equation given above, it is possible to derive all the charge transport parameters, notably, the net mean velocity $\langle \vec{v} \rangle = \langle \frac{\nabla_k \mathcal{E}}{\hbar} \rangle$, also referred as drift velocity v_d, defined as the first moment of the distribution density *f*. The entirety of the demonstration is beyond the purpose of this thesis. However, we will briefly comment on the results in the isothermal and uniform approximation, as they introduce some quantities that will be relevant for the rest of the discussion.

The first notable result is that the drift velocity of the charge carriers is directly proportional to the applied field:

$$\boldsymbol{v_d} = -\frac{e\tau}{m} \boldsymbol{E} \tag{1.5}$$

where the proportionality factor $\frac{e\tau}{m}$ takes the name of electrical mobility μ. We can recall the definition of the current density $\boldsymbol{J}$ and rewrite the expression in terms of the mobility and the relaxation time τ:

$$\boldsymbol{J} = -en\boldsymbol{v_d} \qquad \boldsymbol{J} = \frac{e^2 n\tau}{m} \boldsymbol{E} = \sigma \boldsymbol{E} \qquad \sigma = en\mu \tag{1.6}$$

Since the electric field, drift velocity and current density are vectors usually defined in three dimensions, it follows naturally that both μ and σ are tensors in the general case. In summary, mobility and scattering time are the necessary and sufficient parameters to give a complete description of the properties of the conductor or semiconductor of choice. In the next sections, we describe in more detail the more interesting case of charge motion in materials exposed to an oscillating electric field.

1.1.1 Classical electron gas: Drude model

One of the crudest, yet effective models to explain charge carrier motion in a conductor is the Drude model.[2] In this theory, charge carriers are treated classically and it considers valence electrons belonging to the outer shells as a nearly free, independent electron gas that interacts only with the positively charged background, represented by the ion lattice. This interaction can be described as a collision, which has the effect of randomizing the momentum of a single electron, interrupting its otherwise ballistic motion. These random scattering events occur with a mean rate that we set equal to τ^{-1}. When the gas is placed in an electric field $\boldsymbol{E}$, we can write the equation of motion of a single charged particle as

$$\frac{d\boldsymbol{p}}{dt} = -\frac{\boldsymbol{p}}{\tau} - e\boldsymbol{E} \tag{1.7}$$

where $\boldsymbol{p}$ is the momentum of the particle and e represents the elementary charge. We consider an oscillating electric field $\boldsymbol{E}(t) = \boldsymbol{E}(\omega)e^{-i\omega t}$ and we seek a steady-state solution for the momentum of the form $\boldsymbol{p}(t) = \boldsymbol{p}(\omega)e^{-i\omega t}$. If we substitute these expressions for $\boldsymbol{E}$ and $\boldsymbol{p}$ into (1.7), we obtain that the electric field and momentum must obey

$$i\omega\boldsymbol{p}(\omega) = \frac{\boldsymbol{p}(\omega)}{\tau} + e\boldsymbol{E}(\omega) \tag{1.8}$$

With this result, we can rewrite the current density $\boldsymbol{j}(\omega)$ as

$$\boldsymbol{j}(\omega) \coloneqq \frac{ne\boldsymbol{p}(\omega)}{m} = \frac{ne^2\tau}{m} \cdot \frac{\boldsymbol{E}(\omega)}{1 - i\omega\tau} \coloneqq \hat{\sigma}_D(\omega)\boldsymbol{E}(\omega) \tag{1.9}$$

where n is the carrier density. The proportionality factor $\hat{\sigma}_D(\omega)$ is the complex Drude conductivity

$$\hat{\sigma}_D(\omega) = \frac{ne^2\tau}{m} \cdot \frac{1}{1 - i\omega\tau} \tag{1.10}$$

In the case of semiconductors, we can replace the electron mass with the effective mass m^* given by the band structure of the system:

$$\hat{\sigma}_D(\omega) = \frac{ne^2\tau}{m^*} \cdot \frac{1}{1 - i\omega\tau} \tag{1.11}$$

The Drude model has been successfully employed to explain the conductivity spectra of metals, semimetals and crystalline inorganic semiconductors, however the picture of the interaction with the positive background was falsified as a result of the Bloch's theorem, which proves that a charge cannot be scattered by a periodic potential, *i.e.* the ion lattice. Without a relaxation time, that in the case of the Drude model is determined by electron-ion collision, the conductivity of the material should be infinite. The results of the Drude model were recovered in 1928, when Sommerfeld published his semiclassical theory of an electron gas that obeys the Fermi-Dirac statistics.[3] Within Sommerfeld's approximation, only the electrons with an energy in proximity of the chemical potential of the Fermi-Dirac distribution take part in the conduction and the impurities included in the material, instead of the ion lattice, have to be considered responsible for electron scattering.

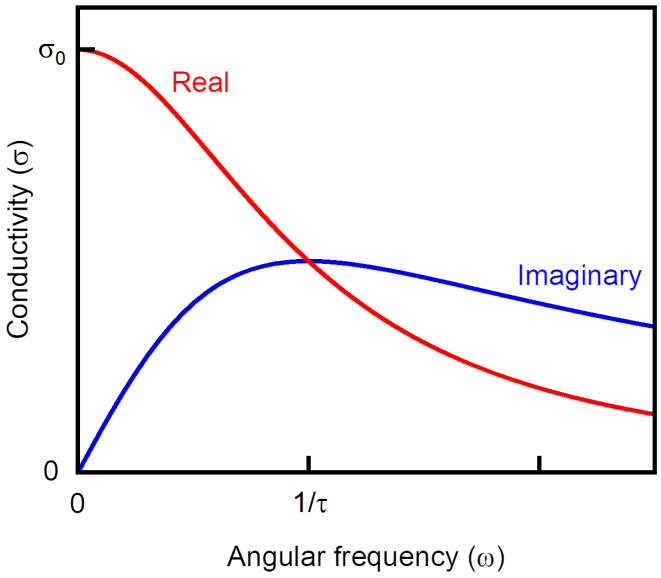

Figure 1.1: Drude conductivity as a function of angular frequency. The real (red) and imaginary part (blue) cross at a frequency equal to the scattering rate τ^{-1}.

1.1.2 Localization effects on Drude conductivity: Drude-Smith model

When inhomogeneity or extended defects play a relevant role in a material, *e.g.*, grain boundaries or mixture segregation, we observe a drop of the conductivity at low frequency that is representative of a suppression of the long-range charge transport. In this scenario, the Drude model can not describe experimental values for the conductivity. A solution to this problem was introduced by N. V. Smith to explain the conductivity of liquid mercury.[4] The model he developed considered that a carrier could

undergo preferential backscattering after a collision.

$$\hat{\sigma}_{DS}(\omega) = \hat{\sigma}_D(\omega)\left(1 - \sum_{s=1}^{\infty} \frac{c_s}{1 - i\omega\tau}\right) \tag{1.12}$$

where c_s denotes the probability of a backscattering event after the s collision. In other words,the terms c_s are the expectation value of $\cos(\theta)$, where θ is the angle between the momenta before and after the scattering event. The series is normally truncated to the first term, as if the carrier experiences a preferential backscattering only during the first scattering event. The formula then becomes

$$\hat{\sigma}_{DS}(\omega) = \hat{\sigma}_D(\omega)\left(1 - \frac{c}{1 - i\omega\tau}\right) \tag{1.13}$$

which recovers the Drude conductivity of (1.11) for $c = 0$.

Although the formula manages to describe fairly well experimental data, the assumption that leads to the truncation of the series in (1.12) lacks of a rigorous justification. Another issue of this model is the assumption that the rate in the parentheses of equation (1.13) is equal to the standard, bulk, Drude collision rate. These considerations have exposed the Drude-Smith formalism to a certain degree of criticism.[5, 6] As a consequence, the model has been applied only as a phenomenological description to a plethora of different systems that could include weak charge confinement, ranging from nanosystems to organic semiconductors.

1.2 Inorganic semiconductors

The first class of semiconductors that we consider in this thesis is represented by crystalline solids. In the following sections, we first derive the behavior of electrons in the crystalline semiconductors with a particular focus on the bandgap opening, before going into more details on the topic treated in Chapter 3, such as solar cells and chalcopyrites semiconductors.

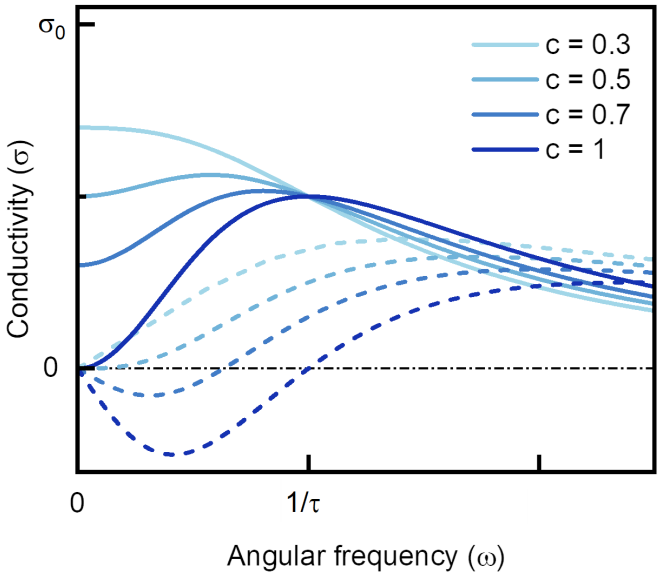

Figure 1.2: Real (solid lines) and imaginary parts (dashed lines) of the Drude-Smith conductivity as a function of angular frequency, plotted for several values of the parameter c. Note that for $c > 0.5$, the imaginary part assumes negative values at low frequencies.

1.2.1 Band structure

The problem of electrons in a solid is in general a many-electron problem, and it is impossible to solve exactly. One way to simplify the problem is to consider electrons to be independent and adopt restrictions on the potential, reasonably assuming that it is periodic on the lattice. In this way, in the one-dimensional case, following Bloch's theorem, the solutions of the stationary Schrödinger equation for a single electron takes the form

$$\Psi(r) = \sum_k c_k e^{ik \cdot r} \tag{1.14}$$

Where the summation in (1.14) is performed over all k crystalline wave vectors, which are permitted by the periodic boundary conditions. In a one dimensional crystal with lattice constant a and a total number of unit cells N, the possible k-values that can be assumed in the Brillouin zone are also N, spaced from each other by an amount $\frac{2\pi}{Na}$. We can introduce the vectors K of the reciprocal lattice and rewrite (1.14)

$$\Psi(r) = e^{ik\cdot r} \sum_K c_{k-K} e^{iK\cdot r} = e^{ik\cdot r} u_k(r) \tag{1.15}$$

in which $u_k(r) = u_k(r+R)$ is a Bloch function that is invariant upon translation of a vector of the Bravais lattice R. We can substitute $\Psi(r,k)$ this into the Schrödinger equation, the $u_k(r)$ are determined by the eigenvalue problem

$$H_k u_k(r) = \Big[-\frac{\hbar^2}{2m}(k - i\nabla)^2 + V(r) \Big] u_k(r) = \mathcal{E}_k u_k(r) \tag{1.16}$$

Since k is only a parameter of the Hamiltonian and the problem is essentially analogous to a *particle-in-a-box* quantum mechanical system, we expect an infinite set of discrete n solutions, periodic in K, that are continuous in k.[7] We refer at this n distinct solutions as energy bands.

Without the potential $V(r)$, (1.16) returns the trivial solution of plane waves, *i.e.* $\mathcal{E}_k$ has a parabolic dependence on the parameter k (Figure 1.3). Given the system's periodicity, the solutions assume degenerate energy values at the boundaries of the Brillouin zone. However, when we introduce a weak potential, we are subject to the conditions of von Neumann-Wigner or avoided crossing theorem. This theorem states that two eigenvalues of a quantum observable, depending on N continuous parameters, cannot assume equal values unless on a N-2 dimension manifold. In our case, the continuous parameter that we have to consider is precisely k. In practice, this theorem assures the opening of a band gap at the edge of every Brillouin zone. Notably, the weak periodic potential has its major effect on those free-electron levels whose wave vectors are close to the zone

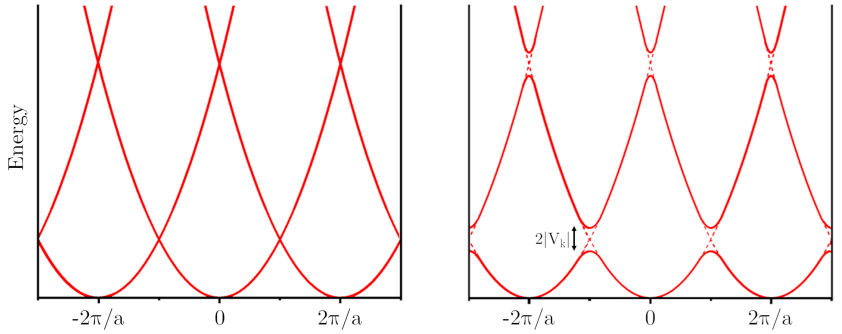

Figure 1.3: Band structure predicted by the nearly free electron theory in absence of potential (left) and with a potential $V(r)$ that opens a prohibited energy gap in corrispondence of bands' crossing points (right).

edge, where the Bragg reflection occurs.

At this point, we have a description the band structure of crystalline solids but we did not explore the difference between metals and insulators. In this regard, we have to consider how many electrons the system provides for each unit cell. Earlier, we have mentioned that we have a crystal with N unit cells is characterized by the same amount of distinct k-vectors, equally spaced within the interval $-\frac{\pi}{a} \leq k \leq \frac{\pi}{a}$. The number of states is then $2N$ because of the electron spin multiplicity. We can imagine filling the bands with electrons until a specific value that has been historically defined as the Fermi energy E_{F}. At absolute zero, if every unit cell contributes with an odd multiple of one electron, the result is a half-filled band, that corresponds to a metallic behavior of the system. In turn, if the number of electron per unit cell is a multiple of $2N$, the bands will be completely full up to an energy value equal to E_{F} and empty above it. This is the situation describing insulators. In this last case, the last filled band is referred to as the valence band (VB), while the first unoccupied one is called the conduction band (CB).

Since every energy level within a band is occupied in an insulator, an

electric field cannot transfer momentum to an electron in the VB and consequently induce a current. To give to these the ability to conduct electricity, it is necessary first to provide enough energy to an electron to be promoted into the CB. When the requirement corresponds to the energy provided by an infrared or visible photon, *i.e.* $< 3\,\text{eV}$, we usually talk about semiconductors instead of strict insulators. This is usually thanks to the fact that in the case of semiconductors is reasonably straightforward to optically excite some electrons to the CB to control the resulting conductivity, *i.e.* the photoconductivity, of the material under examination.

At a finite temperature T, the band occupational state is described by Fermi-Dirac statistics. In practice, this means that a small fraction of electrons, depending on the width of the energy gap, can be thermally excited from the VB to the CB, leaving empty states behind. The absence of an electron in the CB is effectively a state that can be occupied by another particle that of the same band that is accelerated by an electric field, contributing to the overall conductivity. It is more intuitive to think of this empty state, a *hole* as a positively charged particle that behaves in analogy to the negatively charged electron. For this reason, it is necessary to consider the conductivity in semiconductors as the sum of both electrons (σ_e) and holes conductivity (σ_h).

$$\sigma = \sigma_e + \sigma_h \tag{1.17}$$

By this construction and for obvious charge neutrality requisites, for each excited electron in the CB, either thermally or after the absorption of a photon, must correspond a hole in the VB. We call this condition an intrinsic semiconductor.

1.2.2 Solar cells

An important feature of semiconductors is that it is possible to introduce a small amount of extrinsic defects to substantially influence the material's electronic properties. This process is known as doping. The concept behind

doping is to introduce a shallow defect very close to one of the band edges of the semiconductor, so that it is completely ionized at the targeted working temperature of the device, with the net effect of promoting a charge into an energy band, where that charge becomes available for conduction. When the doping element donates electrons to the CB we refer to n doping. In the opposite case of a dopant that introduces holes to the VB we talk about p-type doping. Whilst being electrically neutral, an n-type semiconductor is characterized by an excess of electrons. Analogously, a p-type doped material is unbalanced toward a larger concentration of holes. If we put two materials in contact, one with p and the other with n doping, there will be a migration of electrons from n to p and vice versa for the holes, creating what is called a *depletion region*. The flow is dictated by the concentration gradient of the two species. A dynamic equilibrium is enforced by the electric field that results from the charge imbalance. The structure that forms when putting in contact materials with the two different doping types is called a p-n junction, and it is the fundamental component of all electronic devices.

One of the first application of the p-n junction, dating even back to 1883, is the solar cell,[8] a device based on the photovoltaic effect of a junction, which was first observed in a semiconductor in 1876.[9] In short, upon the absorption of a photon, the electric field in the p-n junction separates the photogenerated electron-hole pair, building a current that can be used to extract work (Figure 1.4). Nowadays, solar cells have become a reliable and consolidated technology for energy production and one of the multiple solutions in the race to overcome our need for fossil fuels. The photovoltaic market is currently dominated by silicon-based devices, which represent roughly 80% of the installed capacity.[10] Silicon panels have become widespread by taking advantage of the technology developed for electronic chip manufacturing industry. This has allowed scaling up production volume and quality, while reducing the costs at the same time. Silicon is usually referred as the first generation of solar cell technology.

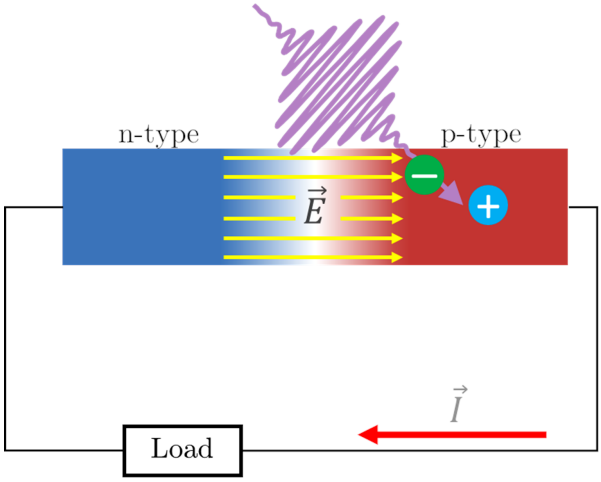

Figure 1.4: Basic working principle of a solar cell. After electron and hole photogeneration, the charge carriers are separated by the electric field $\vec{E}$ present around the depletion region. The separation builds a current $\vec{I}$ used to extract work at the load.

Despite being the most common material for solar cells by far, silicon is not the best one available from purely efficiency perspective. The two main reasons originate directly from the band structure of the crystal itself. First of all, silicon has an indirect band gap, *i.e.* the absorption of a photon has to be assisted by a lattice phonon and becomes a three-body problem. This requirement translates into a relatively low absorption coefficient and into the need for thicker, heavier, and therefore more expensive active layers. Secondly, the width of the energy gap in silicon is 1.1 eV, approximately 0.2 eV lower than the optimal bandgap for a single-junction solar cell.

The optimal bandgap for a solar converter is defined by the Shockley-Queisser (SQ) detailed balance limit.[11] To understand this, we have to consider that a material is transparent to the radiation characterized by photons with energy lower than the bandgap, while on the other hand the charges generated well above the band edge dissipate their energy

effectively before being collected by the electrodes. This results in a trade-off between the number of collected charges and their energy. As a consequence, under terrestrial conditions, the maximum power that can be extracted by a device reaches an optimal value of 31% when the energy gap is equal to 1.34 eV. With the expression terrestrial condition, we refer to the fact that we consider the solar spectrum after the absorption and dispersion losses due to the presence of the Earth's atmosphere. The concept of the SQ limit and available spectral losses are represented in Figure 1.5.

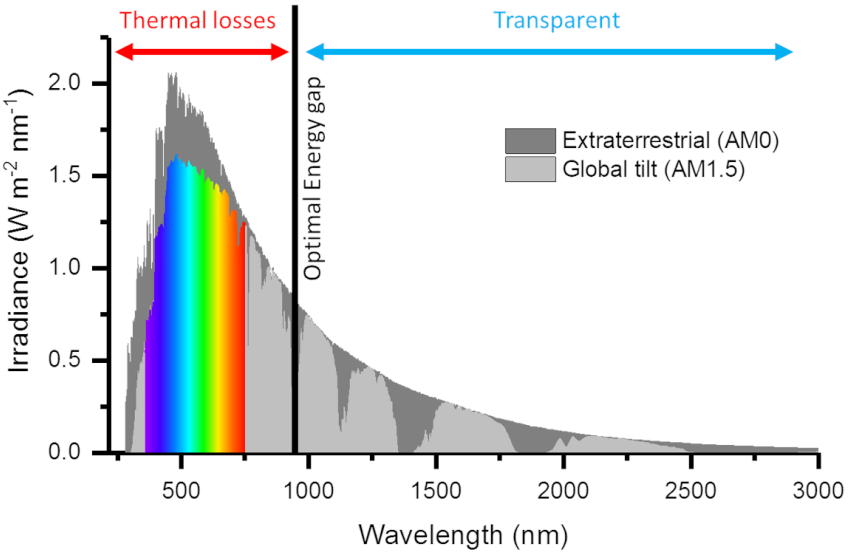

Figure 1.5: Representation of the causes of the Shockley-Queisser limit. Solar irradiance of light above the energy gap of the material undergoes to thermal losses when absorbed, while the device is transparent to the below-gap photons. The solar energy spectra are extracted from data provided by the National Renewable Energy Laboratory (NREL).[12]

One other major issue of first generation solar devices is that we need an enormous amount of energy to grow a crystal of sufficiently high quality.

For all of the reasons we listed, there is constant search for a cheaper solution without a dramatic trade-off in performance.

One possible strategy to differentiate from the dominant Si market is to go for a material with a direct band gap. Thanks to this property, the transition of electrons from valence to conduction band through optical absorption is stronger compared to the indirect gap situation. The immediate result is that the absorption coefficient of the material increases, so that a thinner active layer is sufficient to absorb an amount of light equivalent to the Si competitor. In the photovoltaic industry, this is referred as thin-film technology, or second generation. In this family, the most prominent members in terms of current market share and installed power are amorphous silicon (a-Si), cadmium telluride (CdTe) and copper-indium-gallium-diselenide (CIGS).[13]

1.2.3 Thin film photovoltaics: CIGS

CIGS solar modules combine the advantages of thin-film technology with the efficiency and reliability of conventional first generation modules. In fact, the typical CIGS layer in commercial solar cells is 2 µm thick, about a hundred times less than a crystalline silicon one, with a comparable efficiency despite the youth of the technology.[14, 15] The core of the state-of-the-art CIGS solar cell is a heterojunction between the p-type quaternary alloy and n-type cadmium sulphide (CdS), topped with a transparent zinc oxide (ZnO) and with a back metallic contact of molybdenum.

The main advantages over the real top player in photovoltaics are the possibility of a better architectonic integration and the lower temperature necessary for the manufacturing of the device. While silicon wafers require a temperature in excess of 1100 °C, CIGS can be grown in a range between 450 °C to 550 °C. Specifically, thanks again to both the minimal thickness and low-temperature processing, it is possible to fabricate CIGS modules grown on flexible substrates, which can adapt to various surfaces.[16]

On the other had, the disadvantages include the scarce Earth abundance

of elements such as gallium or indium and a cost that is still too high to effectively compete with the well-established silicon technology. Part of the research nowadays consists also in finding alternatives to indium and gallium, to overcome the limited availability.[17, 18]

In addition, the maximum efficiency achievable for the single junction is theoretically higher compared to silicon, given the possibility to tune continuously the energy gap from 1.1 eV to 1.7 eV, with a progressive substitution of indium with gallium in the alloy. However, as we will discuss more in detail in Chapter 3, increasing the gallium content above a certain threshold, results in a drop in the device efficiency instead of the expected increase.

1.3 Organic semiconductors

The history of modern organic semiconductors (OSC) can be dated back to 1977, when Shirakawa, Heeger and MacDiarmid published the discovery of a highly conductive doped *trans*-polyacetylene, which was subsequently awarded with the Nobel Prize in chemistry in the year 2000. This early work demonstrated that polymers could be used as active materials and marked the beginning of organic electronics.[19] This class of materials is particularly desirable as an alternative to the inorganic semiconductors in every case the cost reduction is a priority. Far from being just a mere cheap alternative, carbon-based systems possess unique features like the relative ease of energy levels tuning and chemical selectivity.

The electronic properties of our interest in this thesis, are essentially determined by the hybridization of the carbon atoms that constitute the backbone of the material. In fact, while saturated sp^3 organic systems generally show insulating behaviour, sp^2 hybridized molecules can exhibit a semiconducting or even metallic properties thanks to the unbound electron in the p_z orbital of each carbon atom.[20]

1.3.1 Conjugated polymers

We can describe the wavefunction and energy of the system, according to the *tight binding* approximation and the Hückel method. Although the model may be considered an oversimplification of the case of study, it serves the use to provide a correct physical intuition about the functioning of conjugated polymers. We consider only the π electrons in the p_z orbitals, along the axis perpendicular to the C–C backbone, since they are the ones responsible for the optical and electronic properties in conjugated molecules.

Band structure of polymers

We take first in exam the generic electronic Hamiltonian $\mathcal{H}$:

$$\mathcal{H} = -\frac{\hbar}{2m}\sum_i \nabla_i^2 - e^2\sum_\nu\sum_i \frac{Z_\nu}{r_{\nu i}} + e^2\sum_{i<j}\frac{1}{r_{ij}} \tag{1.18}$$

where the first term represents the kinetic energy, the second is the coupling between the i electron and the ν nucleus and the latter is the electron-electron coupling term. This last element can be neglected under the assumption of non-interacting electrons. Consequently, the total Hamiltonian then becomes the sum of single electron Hamiltonians:

$$\mathcal{H} = \sum_i H_i = \sum_i [-\frac{\hbar}{2m}\nabla_i^2 + h_i] \tag{1.19}$$

An additional simplification is to write the system wavefunction Ψ, which are solution of the stationary Schrödinger equation, as a linear combination of atomic wavefunction φ:

$$H_i\Psi_i = E_i\Psi_i \qquad \text{with} \qquad \Psi_i = \sum_j c_{ij}\varphi_j \tag{1.20}$$

The coefficients c_{ij} represent the weight of each atomic orbital on the total molecular wavefunction and they are not known *a priori*. One method to evaluate them is to invoke the variational principle to minimize the total energy, hence:

$$\frac{\partial E}{\partial c_{ij}} = 0$$

The energy E is defined as the expected value of the Hamiltonian operator that acts on the eigenfunctions Ψ:

$$E = \frac{\langle \Psi | H | \Psi \rangle}{\langle \Psi | \Psi \rangle}$$

where we can omit the index i, since the equality holds for every eigenfunction. Then, substituting (1.20), we obtain

$$E = \frac{\left\langle \sum_j c_j \varphi_j \middle| H \middle| \sum_s c_s \varphi_s \right\rangle}{\left\langle \sum_j c_j \varphi_j \middle| \sum_s c_s \varphi_s \right\rangle} \tag{1.21}$$

We redefine now

$$H_{js} = \langle \varphi_j | H | \varphi_s \rangle \qquad\qquad S_{js} = \langle \varphi_j | \varphi_s \rangle$$

that take the name of Coulomb and overlap integral, respectively. Thus, Eq.(1.21) becomes

$$E = \frac{\sum_j \sum_s c_j^* c_s H_{js}}{\sum_j \sum_s c_j^* c_s S_{js}} \tag{1.22}$$

following which, according to the variational principle, we obtain a set of j secular equations

$$\sum_s H_{js} c_s - E(S_{js} c_s) = 0 \tag{1.23}$$

Now it is the moment to introduce some additional working hypotheses, which were first published by Hückel:

- $H_{jj} = \alpha$;

- $H_{js} = \beta_{js}$ for any pair of atoms j and s that share a chemical bond;
- $H_{js} = 0$, for any atom j and s that are not chemically bonded together;
- $S_{js} = \delta_{js}$, since atomic orbitals are orthonormal by construction.

In summary, we now have a nearest-neighbor model with the integrals α and β_{js} as parameters to be determined from *ab initio* calculations. It is worth mentioning that both α and β are negative quantities since they originate from an attractive coulombic potential. The system of equations is then reduced to

$$(\alpha - E)c_j + \sum_{j \neq s} \beta_{js} c_s = 0 \tag{1.24}$$

where j runs on all the atoms that constitute the molecule under examination. We will now apply this formalism to calculate the band structure of linear conjugated polymers, in particular starting from the case of polyacetylene.

The case of polyacetylene

Let assume the case of the ideal polyacetylene, a linear periodic chain of N sp^2 hybridized carbon atoms. At first, we consider one atom per unit cell of periodicity a and one electron in the p_z orbital, oriented orthogonally with respect to the direction of the linear chain. Since the system has a distinct periodicity, we can call Bloch theorem to write the polymer wavefunction $\Psi(\vec{r}, k)$ as a combination of Bloch atomic orbitals:

$$\Psi(\vec{r}, k) = \sqrt{N} \sum_j e^{ikja} \varphi(\vec{r} - ja) = \sqrt{N} \sum_j e^{ikja} \varphi_j \tag{1.25}$$

Where k denotes a vector in the reciprocal space. Note that in this case, the coefficients c_j are forced by the Bloch conditions to be on the form $\sqrt{N} e^{ikja}$. In polyacetylene, the j atom is bonded only to the $j \pm 1$ so all the matrix elements relative described by the other indexes are equal to

zero. We take $j = 0$, and then we subtitute into (1.24) to get the energy band structure of the system

$$\begin{aligned} &(\alpha - E)e^{ik0a} + \beta e^{ika} + \beta e^{-ika} = 0 \\ &E = \alpha + 2\beta\cos(ka) \end{aligned} \tag{1.26}$$

with the wavenumber k ranging from 0 to the edge of the Brillouin zone $\frac{\pi}{a}$. Since we have N electrons (one per atom) and therefore $2N$ states due to spin degeneracy, this energy band is half-filled and should show a metallic behaviour.

From the band structure we can calculate the effective mass

$$m^* = \hbar^2 \left(\frac{d^2 E(k)}{dk^2} \right)^{-1} = -\frac{\hbar^2}{2\beta a^2 \cos(ka)} \tag{1.27}$$

A conclusion of utmost importance for molecular electronics that we can derive from relation (1.27) is that the effective mass of the charge carriers is inversely proportional to the overlap integral β. One way to reduce m^* and improve the mobility along the polymer chain is to increase the orbital overlap between nearest neighbours, for example, by controlling the degree of planarity of the molecule. This roughly predicts that more rigid and flatter systems show better conductivities.[21]

From metals to semiconductors

Up to this point, we have considered conjugated polymers as having a single characteristic bond length that defines all the electronic properties of the material. This, of course, is an oversimplification required to understand the general system. In a second approximation, polymers are affected by what is known as Peierls' distortion, which introduces a dimerization of the otherwise uniform chain, opening a bandgap in the proximity of the Fermi surface (Figure 1.6). Any sinusoidal potential of a given amplitude leads to an energy gap opening in the one-dimensional, single-electron energy spectrum.[22] In the ground state, the magnitude

of the phenomenon reaches its maximum when the number of electrons equals the number of levels below the gap. This requires the period of the potential to correspond to a wavenumber that is double the Fermi k-vector at absolute zero ($2k_F$).

Peierls' distortion applies to every 1D periodic potential, but it is normally so weak that it is not observed unless at cryogenic temperatures. It is relevant in organic materials even at room temperature because of the relatively large electron-phonon coupling.[23] This dimerization explains the observation of the alternating single and double bonds in sp^2 systems and is the reason why linear conjugated polymers generally behave as semiconductors with a bandgap that can easily exceed 1.5 eV.

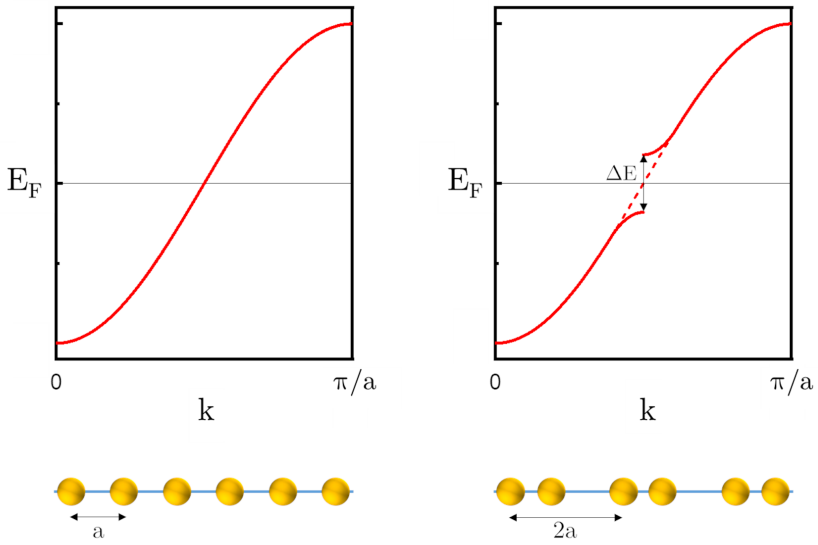

Figure 1.6: Representation of a 1D system that undergoes to Peierls' instability and dimerization, with a gap opening in the middle of the band.

1.3.2 Electronic doping and polaron conductivity

At this point, we have shown that 1D organic systems are substantially insulators, given the bandgap opened by Peierls' instability. The subsequent step to fabricate a device in analogy with their inorganic counterpart, is to find a suitable way to dope the material to tune its Fermi energy and alter the properties of either electrons and holes. In inorganic semiconductors the doping is usually achieved by substituting one atom in the lattice that adds a shallow defect state close to either the valence (p-type doping) or the conduction band (n-type doping) that is completely ionized at the device working temperature. The net result of doping is thus introducing a conspicuous amount of charges that boosts the conductivity at the expense of a minor mobility drop due to the presence of shallow defects. In organic material, on the other hand, the picture presents some complications.

One of the most important breakthroughs in the organic semiconductor (OSC) field, was the discovery that the exposure of polyacetylene to either oxidizing or reducing agents, *i.e.* to substances that add or remove an electron from the polymer chain, can result in an eight orders of magnitude increase in conductivity.[19, 24] The result of this redox operation is what we call doping. Doping in organics can be performed by the inclusion of both single atoms or molecules in the moiety. The requirement to be called a dopant is that the substance does not break up the covalent structure of the OSC. An advantage of OSC is the possibility of after-synthesis and reversible doping at room temperature which make them again radically different from inorganic semiconductors, for which one is restricted to doping during the synthesis, without the possibility of post-processing.[20] It has traditionally been assumed that the doping mechanism is in complete analogy with the inorganic case, with an integer charge transfer from the highest occupied molecular orbital (HOMO) of the OSC to the lowest unoccupied molecular orbital (LUMO) of the p-dopant, and vice versa for n-type doping. Mutual ionization, however, does not always occur,

and more recently, it has been shown that doping can be achieved via hybridization of the frontier orbitals between the pristine OSC and the dopant species.[25, 26]

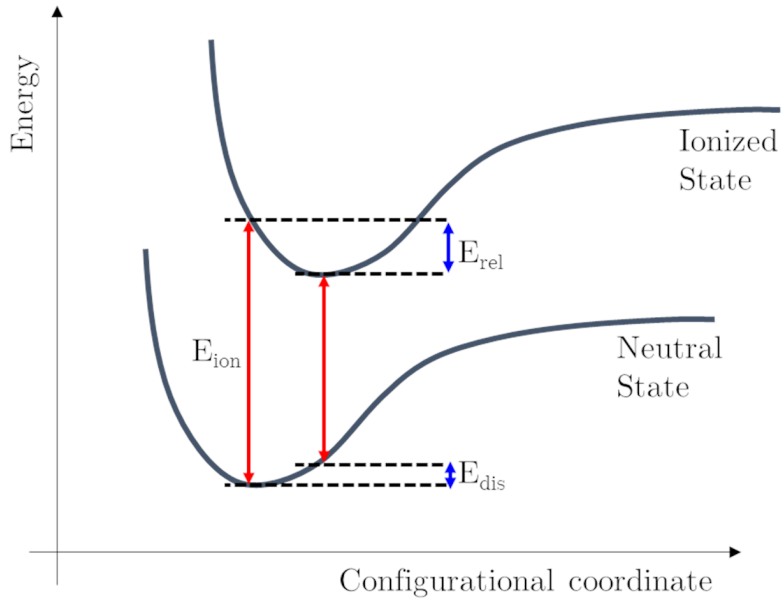

Figure 1.7: Jablonski diagram representing the energetics of the addition of a charge in a molecule.

There is another major difference between polymers and inorganic crystals, but to explain it we have to analyze what happens when a charge is placed on the conjugated backbone of an organic molecule. In an inorganic semiconductor, when we inject an electron into the conduction band, whether via doping or other methods its wavefunction becomes delocalized and spreads across the periodic potential. On the contrary, here is usually a gain in terms of energy in organic molecules if this injected charge is localized to a certain extent. With a vertical transition, we would

provide to the system an amount of energy E_{ion} to ionize the molecule (Figure 1.7). However, the geometry of an ionized molecule can differ from the one of the neutral ground state. This allows the molecule to pay a certain amount of elastic energy E_{dis} in the ground state to rearrange in the new ionized configuration. In return, this new geometry allows for lowering the energy of the electronic system through a relaxation E_{rel} that depends on the coupling between the charge itself with conformational degrees of freedom and the vibrational modes of the system.[24] In this situation, the energy that is needed to ionize the molecule is reduced by

$$\Delta E = E_{\text{ion}} - E_{\text{rel}} - E_{\text{dis}} \tag{1.28}$$

If $\Delta E > E_{\text{dis}}$, then the system would rather distort the lattice around the charge than promote it directly to a delocalized conduction band. We then obtain the formation of states in the middle of the prohibited energy gaps known as polarons. E_{rel} can also be seen as a polaron binding energy, defining how much the polaron wavefunction can extend on the polymer chain. High polaron binding energies result in a deeply localized particle, whilst loosely bound ones tend to be more delocalized. In synthesis, we can describe a polaron as a particle characterized by an elementary charge $\pm e$ and a half-integer spin like an electron or hole surrounded by a local deformation.

The motion of a polaron in an electric field depends on the degree of self-confinement and can be divided into two limiting cases. If the binding energy largely exceeds the thermal energy kT, the charge has little probability of exciting the potential well and waits for tunnelling events to move to adjacent sites. This picture refers to the regime of *strong confinement* or *strong coupling* if we focus on the process that generated the localization. On the complete opposite, we talk about *weak confinement* or *weak coupling* when the potential well is particularly shallow, on the order of kT. In this case, the charge is barely affected by the confinement and can be treated, *e.g.* in the frame of Drude conductivity. The only effect of

the deformation potential cloud that accompanies the electric charge is to increase the effective mass.[27] These two scenarios are also referred to as small and large polarons respectively, also reflecting the size of the lattice distortion across the polymer.

1.3.3 Polyaniline

One of the earliest conductive polymers to be ever observed is polyaniline (PANI). The polymer exists in various forms concerning the possible combinations of the configurational states of the aromatic rings, as depicted in Figure 1.8. In other words, it is possible to find sections in the benzenoid hybridization state or in the quinoid state. According to the terminology proper to chemistry, benzenoid and quinoid form are usually referred to as reduced and oxidized forms of PANI, respectively. We can

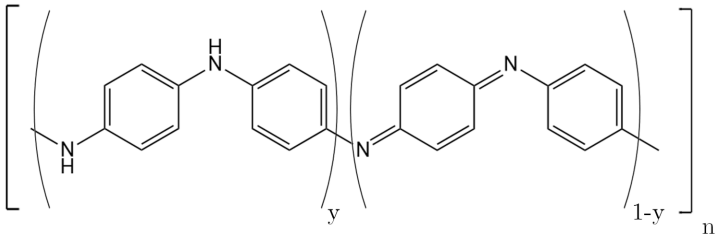

Figure 1.8: Graphical representation of the general form of polyaniline, composed by a ratio of a benzenoid units (left parenthesis) and quinoid units (right parenthesis).

identify three main typologies of PANI on the basis of the ratio between benzenoid and quinoid forms: the fully reduced leucoemeraldine ($y = 1$), the fully oxidized pernigraniline on the opposite end ($y = 0$), and finally the emeraldine base, which is composed of equal number of alternated reduced and oxidized units ($y = 0.5$). Obviously, y is a continuous parameter in high molecular weight polymers, and any linear combination of the three cited forms can be achieved. All of these forms have a closed electronic

shell, and they are thus insulators.[28] However, it is possible to obtain a conductive form of PANI, called emeraldine salt (Figure 1.9), derived from the protonation upon exposure of emeraldine base to protonic acids or, symmetrically, after oxidative doping of the leucoemeraldine.

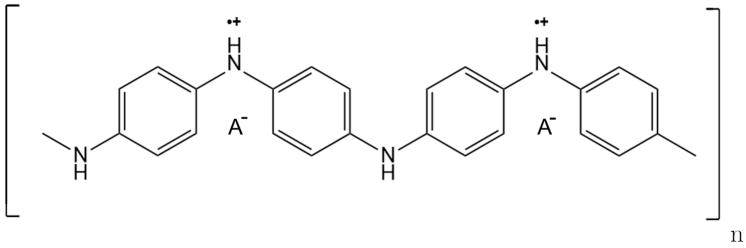

Figure 1.9: Sketched of the fully protonated emeraldine salt. The item denoted by the letter A represents the generic negative counterion to assure charge neutrality.

The protonation of the chain removes an electron from the filled band and induces a polaron lattice deformation in the material, following the concept illustrated in the previous section. The two degrees of freedom, *i.e.* the oxidation level and the protonation level, make PANI substantially different from other OSC, which have conductivity properties that depend on only one parameter: the amount of the doping agent.[29] In Chapter 4 we analyze the doping mechanism and specifically on the effects that a new dopant, phytic acid, has on the conductive properties of PANI thin films.

Chapter 2

THz Time-Domain Spectroscopy

In order to understand the processes that regulate charge carrier transport and dynamics, we need a specific probe able to interrogate the material at the characteristic timescales of those phenomena. In most materials, carrier relaxation and scattering events with the lattice occur in a time window spanning from fractions to hundreds of picoseconds. Therefore, an oscillating electric field in the THz frequency range is therefore a suitable candidate to sample carrier motion.

From the energetic point of view, THz radiation from 0.1 to 10 THz is characterized by photon energies between 0.4 and 41 meV, which are typically below the usual requirements for interband excitations. THz is therefore sensitive to intraband charge carrier motion in solids, bound charges in excitonic systems, but also some rotational and vibrational modes of small molecules, such as water. The THz energy range is, however, comparable with the thermal energy at room temperature, $k_B T \approx 26\,\text{meV}$, which introduces several obstacles to the incoherent detection of THz photon intensity, *e.g.* with a photomultiplier as in visible light detection.

In the following sections, we will describe the basics of the physical processes behind THz generation and detection that have been employed in our experimental setup and the results described in this thesis.

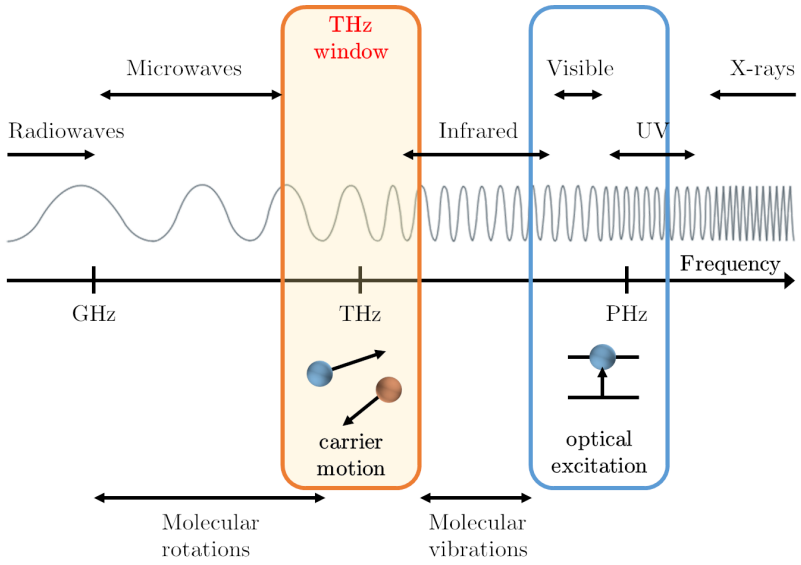

Figure 2.1: Electromagnetic spectrum and the processes stimulated by specific radiation. Highlighted, between microwaves and infrared, the THz window associated with carrier motion.

2.1 THz generation and detection

Since THz frequencies are not achievable with modern electronic equipment, which can reach only up to a few GHz, it was historically challenging to generate radiation in this range. It was only in the 1980s, together with the development of pulsed lasers, that freely propagating THz pulses from photoconductive antennas and optical rectification became widely available.[30] In this chapter, we focus only on the THz generation via optical rectification, as it is the technique that we employed in this work.

Optical rectification consists of a second-order process of light-matter interaction. In the most general case, we can write the polarization density P of a material as a Taylor series in powers of the electric field E

$$P_i = \varepsilon_0 \Big(\sum_j \chi_{ij}^{(1)} E_j + \sum_{jk} \chi_{ijk}^{(2)} E_j E_k + \\ + \sum_{jkl} \chi_{ijkl}^{(3)} E_j E_k E_l + ... \Big) \tag{2.1}$$

where the coefficients $\chi^{(i)}$ are the i-order of the electrical susceptibility tensor of a given material. The first term of the series dominates at low fields and describes electric and optical phenomena such as electric conductivity, absorption, reflection or refraction. Higher-order terms become relevant at high field strengths. Specifically, the quadratic term is responsible for processes like second harmonic generation, sum-frequency generation, This last effect is of our interest for the generation of THz pulses as it is a process that can generate very low-frequency oscillations from a high-frequency laser source. Let us consider the case of a continuous-wave monochromatic laser beam incident on a crystal with non-zero second-order susceptibility $\chi^{(2)}$. We can represent the laser output as a plain electromagnetic wave of angular frequency ω:

$$E(t) = E_0 \cos(\omega t) \tag{2.2}$$

where we simplify (2.1) to a scalar notation for clarity purposes. The resulting second-order polarization becomes:

$$P(t) = \varepsilon_0 \chi^{(2)} E(t)^2 = \frac{\varepsilon_0}{2} \chi^{(2)} E_0 \Big[1 + \cos(2\omega t) \Big] \tag{2.3}$$

Here, the first term in the parentheses is a constant amplitude contribution, while the last term indicates that the material starts oscillating, and consequently radiating, at a frequency that is twice that of the incoming light, describing the second harmonic generation process. This constant term in (2.3) is responsible for optical rectification. If instead we mix two

waves with different frequencies ω_1 and ω_2, Equation (2.3) becomes

$$\begin{aligned} P(t) &= \varepsilon_0 \chi^{(2)} E_1(t) E_2(t) = \\ &= \frac{\varepsilon_0}{2} \chi^{(2)} E_0 \Big[\cos\big((\omega_1 + \omega_2)t\big) + \cos\big((\omega_1 - \omega_2)t\big) \Big] \end{aligned} \tag{2.4}$$

where in complete analogy with (2.3), we have a term with a sum frequency generation, not relevant for our discussion, while the second term deserves more attention for THz generation. Let us consider a pulse, with a Gaussian envelope of the electric field characterized by a time duration Δt. At the same time, through its Fourier transform, the pulse is composed by set of frequencies with bandwith γ^{-1} centred around a value ω_0.

$$E(t) = E_0 \cdot e^{-\frac{(\omega - \omega_0)^2}{\gamma}} \tag{2.5}$$

The generation of THz-radiation pulses is based on difference frequency mixing of all frequencies within the bandwidth $\Delta\omega$ of the short laser pulse. Next, the polarization induced in the non-linear crystal radiates a field that is proportional to the second time-derivative of the polarization.

$$E_{\mathrm{THz}}(t) \propto \frac{\partial^2 P(t)}{\partial t^2} \tag{2.6}$$

Combining (2.5) and (2.6) in the Fourier space, we obtain that

$$E_{\mathrm{THz}}(\omega) \propto \omega^2 \cdot e^{-\frac{\omega^2}{\gamma}} \tag{2.7}$$

In general, we can say that the optical rectification term creates an electric field that possesses the same duration as the field envelope of the incident pulse. If the pulse duration is short enough, on the order of $\sim$100 fs, a Fourier transform reveals that the resulting rectified radiation will contain photons in the THz frequency window. The THz emission bandwidth is then limited on one hand by the duration of the pulse employed to trigger the optical rectification and, more critically, by phase matching

conditions between the driving optical pulse and the rectified THz field in the non-linear crystal that supports the process. In addition to the phase mismatch, the optical properties of the crystal can be responsible of resonances between phononic transitions and the rectified THz radiation, resulting in the absorption of specific frequencies.

A THz pulse generated with the method just described can be measured via linear electro-optic sampling, based on the Pockels effect on a non-centrosymmetric crystal.[31] The THz electric field acts as a bias and triggers a birefringence that induces a small rotation of the polarization of a spatially and temporally overlapped laser pulse, that for the purpose we name *sampling beam*. By using a non-centrosymmetric crystal, the rotation of the polarization is directly proportional to the electric field and not to its square, as the Pockels effect, which depends on the second-order susceptibility $\chi^{(2)}$, dominates over the third-order Kerr effect at low field strengths.[32] After the sampling crystal, the linear polarization is then converted into a circularly polarized light by a quarter waveplate. The horizontal and vertical components of the circular polarization, which we call I_1 and I_2, are subsequently separated by a Wollaston prism and directed to a set of balanced photodiodes. In normal conditions, when the sample is in the ground state, the two polarization components have equal intensities, and the photodiodes measure a total signal $S = I_1 - I_2 = 0$. When the THz field strength is altered, for example after the photoexcitation of a sample, the output of the quarter waveplate becomes slightly elliptical. As a consequence, $I_1 > I_2$ and $S \neq 0$.

The main advantage of electro-optic detection is the time resolution, which is limited by the duration of the sampling beam and the mismatch between optical group velocity and THz phase velocity. With this method, it is therefore possible to resolve a relatively long THz pulse, up to a few ps. The THz field varies on a timescale that is slow compared to the duration of the sampling beam, typically on the order of tens of femtosecond.[33] As such, the sampling beam measures the quasi-instantaneous THz field at any point during the relatively slower THz oscillation. Another consequence of

the time-domain detection of the THz electric field is that with a single measurement, we have direct access to both amplitude and phase of the incoming radiation, in contrast to other techniques that measure a power signal, that is, proportional to the number of photons that reaches the detector. The feature becomes particularly relevant when the signal is translated via Fourier transform into the frequency domain, since the simultaneous availability of both real and imaginary components gives the possibility to avoid a Kramers-Kronig analysis.[6, 34]

2.2 Optical Pump-THz probe

In this work, we use optical pulses to excite the semiconductors to bring them out of equilibrium. The energy of the photons that compose the optical pulse is large enough to overcome the energy bandgap of the sample. Then, after a well-defined delay τ, the THz pulse is introduced as an electric probe and takes a snapshot of the transient status of the material, providing information about the electro-optic relevant quantities such as refractive index or conductivity. This technique is called Optical Pump-THz Probe (OPTP) spectroscopy.

2.2.1 Obtaining the photoconductivity

At first, we can remember the relation between the permittivity of a medium ε with the complex refractive index $\hat{n}$ and the conductivity σ:

$$\hat{\varepsilon} = \varepsilon_1 + i\varepsilon_2 = \hat{n}^2 = 1 + \frac{i\sigma}{\varepsilon_1 \omega} \tag{2.8}$$

We start by considering a plane THz waveform, which propagates through several media described by the respective complex-valued refractive indexes $\hat{n}_j(\omega) = n_j(\omega) + i\kappa_j(\omega)$ and thickness d_j. The transmitted electric

field E after the i region takes generally the form:

$$E_{j+1}(\omega) = E_{j-1} \cdot t_{j-1,j} \cdot e^{in_j k d_j} \cdot t_{j,j+1} \cdot \mathrm{MR}_j \tag{2.9}$$

where $e^{in_j k d_j}$ is the phase that the waveform accumulates while travelling in the j-slab, which we denote now on as p_j. The term MR_j takes into account the multiple reflections in the j-layer:

$$\mathrm{MR}_j = \frac{1}{1 + r_{j-1,j} r_{j,j+1} \cdot p_j^2} \tag{2.10}$$

and finally $t_{j,j+1}$ and $r_{j,j+1}$ are respectively the Fresnel transmission and reflection coefficients between the j and j+1 surface, defined as:

$$t_{j,j+1} = \frac{2n_j}{n_j + n_{j+1}}, \quad r_{j,j+1} = \frac{n_j - n_{j+1}}{n_j + n_{j+1}} \tag{2.11}$$

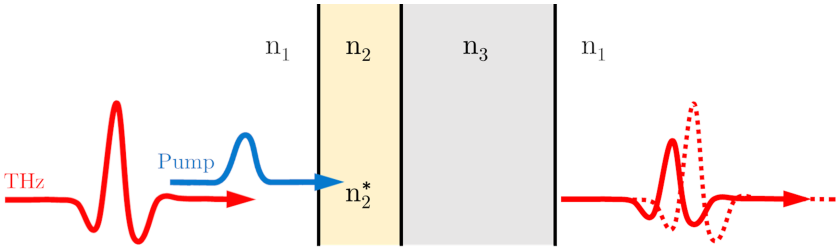

Figure 2.2: Typical sample geometry. n_1 indicates a surrounding medium. The optical pump (blue) excites the active material n_2 that is deposited on a substrate n_3. Then, the THz pulse (red) probes the material in the excited states n_2^*. The dashed line represents the transmitted THz pulse in absence of photoexcitation.

Let us consider the case represented in Figure 2.2 of a thin film described by a refractive index n_2 that is deposited on a dielectric, optically inert substrate with an index n_3. The parameter n_1 is used to represent the surrounding medium, which in most cases refers to air. The transmitted electric field in normal conditions, *i.e.* when it is not excited by the optical

pump, can be written as

$$E_{\mathrm{ref}} = E_0 \cdot t_{12} p_2 \cdot t_{23} p_3 \cdot t_{31} \cdot \mathrm{MR}_2 \tag{2.12}$$

where we emit the initial phase p_1 and the one accumulated after the substrate. For the case of an photoexcited sample, (2.12) becomes

$$E_{\mathrm{exc}} = E_0 \cdot t^*_{12} p^*_2 \cdot t^*_{23} p_3 \cdot t_{31} \cdot \mathrm{MR}^*_2 \tag{2.13}$$

where the new terms t^*_{12}, p^*_2, t^*_{23} and MR^*_2 derive from the only perturbed complex refractive index $n^*_2 = n_2 + \Delta n$.

$$\frac{E_{\mathrm{exc}}}{E_{\mathrm{ref}}} = \frac{t^*_{12} t^*_{23}}{t_{12} t_{23}} \cdot \frac{p^*_2}{p_2} \cdot \frac{\mathrm{MR}^*_2}{\mathrm{MR}_2} \tag{2.14}$$

The corrections for multiple reflections become important only in the case of thin films, *i.e.*, when the THz wavelength is small in comparison with the thickness of the absorber layer. In the opposite case, in fact, the effect of the multiple reflections can be filtered out by an opportunely chosen time window. In the limit of small perturbations of the active layer, so that $\frac{\Delta n_2}{n_2} \ll 1$, we can neglect higher order of Δn_2 it is possible to linearise (2.14) and separate it in the form:[35, 36]

$$\frac{E_{\mathrm{exc}}}{E_{\mathrm{ref}}} = 1 + \Delta n_2 \cdot \left(\frac{1}{n_2} - \frac{1}{n_2 + n_3} - \frac{1}{n_1 + n_2} + ikd_2 \right) \tag{2.15}$$

From (2.15) we can then isolate Δn_2 so that the left term becomes directly proportional to this photoinduced refractive index variation

$$\frac{E_{\mathrm{exc}}}{E_{\mathrm{ref}}} - 1 = \frac{\Delta E}{E_{\mathrm{ref}}} \propto \Delta n_2 \tag{2.16}$$

Following the identity (2.8) we can rewrite in terms of the photoconductivity $\Delta\sigma$ so that

$$\frac{\Delta E}{E_{\mathrm{ref}}} = \Xi \frac{\Delta\sigma}{i\omega\varepsilon_0} \tag{2.17}$$

where we collapsed the proportionality factor between the differential transmission and the photoconductivity to the quantity Ξ, that we can call transfer function or filter. Ξ depends exclusively on the properties of the unexcited system and can be determined independently and known *a priori*.[37] In this way, we can observe how the photoconductivity is directly proportional with the measurable differential transmission of the THz electric field.

Then, we illustrate in Figure 2.3 some of the configurations that are relevant and have been used in this work. In particular, we focus our attention on the ones represented in Figure 2.3b and Figure 2.3c that have been employed in Chapter 4 and 3, respectively.

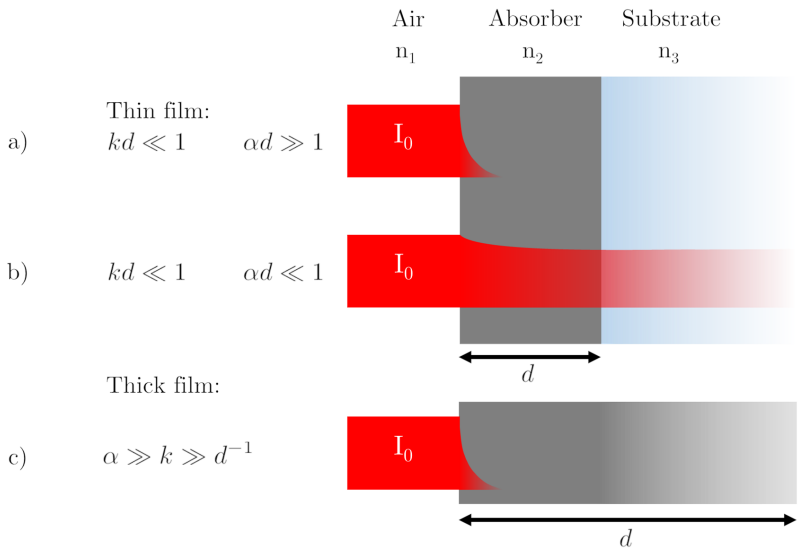

Figure 2.3: Representation of the most common sample geometries found in this work with relative categorization on the base of size and optical thickness. a) Thin absorptive film. b) Thin quasi-transparent film. c) Thick absorptive film.

The first case (Figure 2.3a) consists of a thin, strongly absorptive film, defined by the relation $kd \ll 1$, where k denotes the THz wavevector

and d is the sample thickness and at the same time, described by a light absorption coefficient α, at the excitation wavelength, that satisfy $\alpha d \gg 1$. Under the previous assumptions, equation (2.17) takes the form of:

$$\text{a)} \qquad \Delta\sigma(\omega) = -\alpha \frac{n_1 + n_3}{Z_0} \cdot \frac{\Delta E}{E_{ref}} \tag{2.18}$$

These conditions are usually met in the case of a thin sample of a direct bandgap semiconductors grown on a dielectric substrate.

In the opposite limit of an optically thin sample, $\alpha d \ll 1$, we have:

$$\text{b)} \qquad \Delta\sigma(\omega) = -\frac{n_1 + n_3}{Z_0 \cdot d} \cdot \frac{\Delta E}{E_{ref}} \tag{2.19}$$

with the only difference that it depends explicitly on the film thickness d instead on the penetration depth α^{-1}. Equation (2.19) is a good description for thin dielectric films such as organic semiconductors or metal oxides.

Finally, we introduce the case of a thick absorptive film, that can be represented by self-supporting semiconductor crystals, *e.g.*, a GaAs wafer or even a Si wafer excited well above the band edge.

$$\text{c)} \qquad \Delta\sigma(\omega) = -\alpha \frac{n_1 + n_2}{Z_0} \cdot \frac{\Delta E}{E_{ref}} \tag{2.20}$$

The formula in this last example depends on the refractive index of the unexcited material n_2 and the absorption coefficient α that defines the photoexcited layer.

2.2.2 Carrier dynamics

With the notion of carrier dynamics, we refer to the experiment where one obtains a time evolution of the THz transmission, and therefore of the photoconductivity, as a function of the pump-probe delay time τ. The method consists of fixing the THz sampling time at a certain t_{sam} and scanning the relative pump-probe delay time. Setting the THz

sampling time at two specific positions of the waveform, allows for the recording of the time evolution of different components of the complex photoconductivity.

For instance, if we set t_{sam} at the peak of the waveform, we can monitor the evolution of the transient THz amplitude, which in the limit of small induced absorption and small phase shifts, corresponds to the time evolution of the real part of the photoconductivity. Alternatively, when t_{sam} is set at the first zero crossing after the peak, we are particularly sensitive to any phase shift of the frequency components that form the THz pulse. This second method turns to be helpful to estimate the dynamics of the imaginary part of the photoconductivity.[38]

2.2.3 Conductivity spectra

To measure the frequency response, one has to fix the pump-probe delay time and measure both the THz pulse transmission of the ground state and the photoexcited sample. This is easily doable in the case of slow varying dynamics, *i.e* much slower than duration of the THz pulse. On the contrary, in the case of dynamics that evolve within a few picoseconds, it is not possible to measure the response of the material just by fixing the pump-probe delay time and sweeping only the sampling beam arrival time t. This is exactly because the THz pulse itself has a duration of several picoseconds, thus the leading part of the THz waveform probes the material in a different condition than the trailing part. Experimentally, this can be corrected by keeping constant the relative time difference between the pump and the sampling beam while the whole THz waveform is being scanned.

2.3 Experimental setup

The setup used for all the experiments described in this work is schematically represented in Figure 2.4. It is driven by an amplified Ti:sapphire

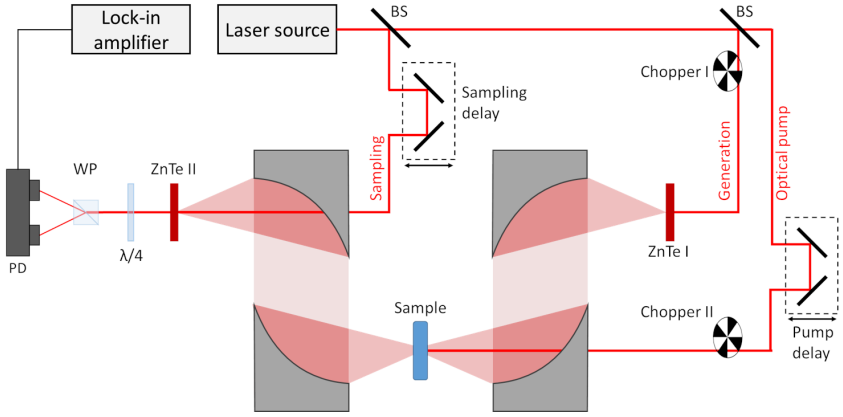

Figure 2.4: Schematic of the THz TDS setup used in this work. BS: beam splitter; WP: Wollaston prism; PD: balanced photodiodes.

laser, capable of producing short pulses of approximatively 50 fs at a wavelength of 800 nm with a repetition rate of 1 kHz. A total power of 1 W is then distributed across three distinct paths that we name as THz generation line, THz sampling line and optical pump line.

The generation beam impinges on a 1 mm (110) ZnTe crystal where, as mentioned early in Section 2.1, we take advantage of optical rectification to generate a pulse with substantial intensity in the frequency range between 0.3 and 2.5 THz. THz radiation emitted from the generation crystal is then collimated and focused on the sample by a series of off-axis parabolic mirrors.

After the sample plane the transmitted THz pulse is redirected toward an identical (110) ZnTe crystal where it interacts with the synchronized sampling beam.

The 800 nm pump beam is used for the photoexcitation of the sample and it can be additionally upconverted to 400 nm by a β-Barium Borate crystal (β-BBO). Alternatively, the output of an Optical Parametric Amplifier (OPA) can replace the original pump line in order to meet

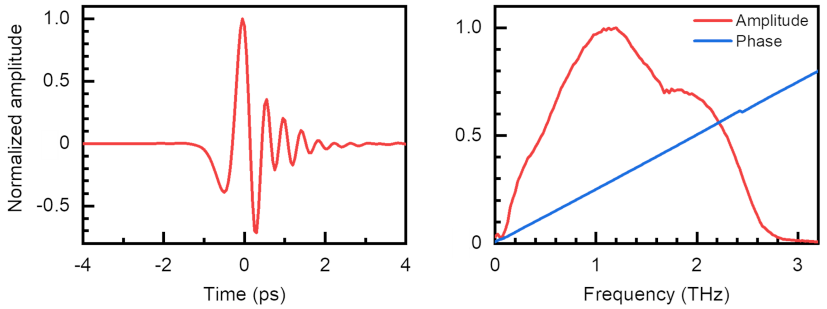

Figure 2.5: Example of the THz pulse measured in our setup and relative spectrum obtained from its Fourier transform.

the required photon energies, from the near-infrared (N-IR) to the near ultraviolet (N-UV). In order to have homogenous pumping, we use a collimated pump with a radius of about 3 mm, substantially larger than the focused THz spot, whose size is essentially limited by the photons' wavelength. The condition of homogenous pumping is particularly crucial when the time window we explore in the experiment is large, as any small misalignment of the pump line could result in a sizeable drift of the spot on the sample plane. To prevent a drop in the photoexcitation and flatten the spot intensity profile, we occasionally place a beam diffuser in the pump path.

To significantly increase the signal-to-noise ratio, two main technical features are implemented. The first is the addition of optical choppers, in order to measure relative differences instead of absolute values. Depending on whether we measure photoinduced changes or THz transmission, either the optical pump or the THz beam is chopped. The second system that is commonly employed is the lock-in detection of the photodiode signals, which allows filtering all the components that are not synchronized with the laser system. This approach opens the possibility to measure THz modulations down to few parts per thousand.

Chapter 3

Carrier dynamics at the CIGS/CdS interface

3.1 Introduction

Chalcopyrite semiconductors based on copper-indium-gallium-diselenide ($CuIn_{1-x}Ga_xSe_2$, CIGS) are currently commercially exploited as light-absorbers in thin-film solar cells.[39] CIGS alloys are an appealing choice for photovoltaics owing to their high absorption coefficient, as a result of their direct bandgap, enabling low-cost thin-film solar cells. In addition, CIGS absorbers can be grown onto flexible, light, and cheap substrates,[40] and have been reported to be more stable under prolonged sunlight irradiation when compared with other competing thin-film technologies such as those based on cadmium telluride (CdTe), amorphous silicon (a-Si), and novel perovskites.[41] A potential additional advantage of chalcopyrites is that the bandgap onset of $CuIn_{1-x}Ga_xSe_2$ quaternary alloys can be easily tuned by controlling the Ga content from $\approx 1.0\,\text{eV}$ (gallium-free, x = 0, i.e., $CuInSe_2$) to $\approx 1.7\,\text{eV}$ (indium-free, x = 1, i.e., $CuGaSe_2$). This feature allows for fine-tuning of the bandgap, which should enable a maximum theoretical photoconversion efficiency of 33.7% at an optimum bandgap of 1.34 eV given by the Shockley–Queisser limit

under an AM1.5 solar spectrum.[11,42]

Remarkably, however, the record ≈23% efficiency of state-of-the-art of ZnO/CdS/CIGS solar cells employ CIGS absorbers with a bandgap of only ≈1.2 eV (Ga content of $x \approx 0.3$),[39,43] *i.e.*, about 0.1 eV below the theoretical optimum.[44,45] This constraint results from the experimental observation that CIGS based solar cells employing Ga contents exceeding $x = 0.3$ undergo a significant reduction in photoconversion efficiency, which is largely driven by an increasing open-circuit-voltage (V_{OC}) deficit relative to the bandgap.[46] The underlying reasons behind the experimentally observed output-voltage saturation of CIGS-based devices with a high-Ga content and its associated efficiency drop have been assigned in literature to different types of mechanisms which can be generally classified into bulk- or interface-limiting factors. Concerning bulk mechanisms, substantial differences in the energetics of point-defect formation of In- and Ga-containing species have been reported, with major penalties predicted for high Ga contents, that might lead to limitations on the maximum achievable splitting of quasi-Fermi levels (and the output voltage of the operating cells) and hampering type inversion of naturally occurring p-type material.[47,48] Additionally, bulk Ga-dependent trapping efficiency of minority carriers has been reported,[49,50] an aspect that might be contributed by a Ga-dependent diffusion efficiency into the bulk of elements like cadmium or sodium,[51,52] which are well-known grain boundary passivators.[53,54] Alternatively, theoretical works have predicted the promotion of metastable light-induced acceptors for high-Ga alloys,[41,52] which are expected to primarily populate the CIGS absorber close to the CdS junction (*i.e.*, primarily a surface effect). Furthermore, Ga-dependent surface effects have been claimed to be responsible for the voltage deficit in state-of-the-art CdS/CIGS interfaces.[55] For example, the absence of an inversion layer at the interface between CIGS absorber and CdS buffer layer for bandgaps >1.2 eV,[43] or the transition from a barrier-like to a cliff-like conduction-band alignment with an increasing Ga content on the absorber side of the interface could explain the poor device performance of wide-gap-

based CIGS devices.[56] Discriminating among these scenarios, therefore, requires disentangling surface from bulk effects on the carrier recombination processes in CIGS absorbers with different Ga content, and their interplay with the CdS buffer layer.

We employ ultrafast photoconductivity measurements with sub-picosecond time resolution to investigate carrier dynamics in air/CIGS and device relevant ZnO/CdS/CIGS interfaces for a set of $CuIn_{1-x}Ga_xSe_2$ samples with Ga contents of $x = 0.3$, 0.5, and 0.7 (with bandgaps of $\approx$ 1.2 , 1.3 , and 1.5 eV, respectively). Our results demonstrate that while bulk charge dynamics are barely affected by the Ga content of CIGS alloys, surface recombination is stronger for higher Ga contents; this aspect is true for both air/CIGS and ZnO/CdS/CIGS interfaces. Notably, we also demonstrate that the CdS surface treatment of CIGS absorbers is only effective in inhibiting surface recombination for low-Ga-containing samples, having a negligible effect on samples with larger Ga contents (*i.e.*, with $x = 0.5$ and 0.7). Finally, we resolve that interfacial recombination at the CdS/CIGS interface increases with photon flux for high-Ga samples, consistent with the formation of metastable acceptors at the interface. Our findings are in line with the observed Ga-dependent efficiency trend in device performance and demonstrate that its origin is linked to surface, rather than bulk-assisted recombination.

3.2 Sample preparation and methods

Two-micrometer thick CIGS absorbers were deposited by coevaporation following a so-called isothermal three-stage pro-cess.[57] The Ga content of the layers (x) was tuned by adjusting Ga/In relative atomic fluxes from one deposition to another. Grown samples are denoted as $CuIn_{0.7}Ga_{0.3}Se_2$, $CuIn_{0.5}Ga_{0.5}Se_2$, and $CuIn_{0.3}Ga_{0.7}Se_2$; associated with a relative Ga content $x = \frac{[Ga]}{[Ga]+[In]}$ equal to 0.3, 0.5, and 0.7, respectively. The CIGS absorbers were deposited on both fused silica and standard Mo-coated soda-lime-glass substrate; the latter batch was used to fabricate

complete solar cells; the solar efficiencies (η) were estimated to be 16.1%, 15.3%, and 11.7% for Ga contents of $x = 0.3$, 0.5, and 0.7, respectively. Up to six samples were deposited onto fused 1 mm thick silica substrates; three of them remained uncovered (air/CIGS samples) and three of them were covered by a 50 nm CdS buffer layer applied by chemical bath deposition and 50 nm ZnO by RF-sputtering from a ceramic target (samples denoted as ZnO/CdS/CIGS).

We performed optical pump–terahertz probe (OPTP) experiments on the six samples consisting of air/CIGS and ZnO/CdS/CIGS structures with three different Ga contents.[33,58] For materials in which the photoexcited layer (l), chosen to be equal to the light penetration depth, is sufficiently thin compared to the sample thickness, it is possible to obtain the photoconductivity of the samples by deriving the following analytic formula that links the measurable THz differential transmission $\left(\frac{\Delta T}{T_{ref}}\right)$ with the transient photoconductivity ($\Delta\sigma$) presented in Section 2.2.1.[59,60]

$$\Delta\sigma = -\frac{n_1 + n_2}{Z_0 l} \cdot \frac{\Delta T}{T_{ref}} \tag{3.1}$$

where $n_{1,2}$ are respectively the refractive indexes, in the THz range, of the medium before and after the photoexcited region, and Z_0 is the free space impedance. In our experiments, the pump light penetration depth at 800 nm was inferred to be 177, 220, and 340 nm for $CuIn_{0.7}Ga_{0.3}Se_2$, $CuIn_{0.5}Ga_{0.5}Se_2$, and $CuIn_{0.3}Ga_{0.7}Se_2$, respectively, based on the data published by Paulson et al.[61] For all the measurements conducted in this study, we observe a linear correlation between the photon flux and the maximum transient transmittance, demonstrating that the carrier dynamics are probed in the linear regime, and that the carrier mobility is independent of carrier density (Figure 3.1). The efficiency of photogeneration right after light pump excitation is resolved to be unity for all samples.

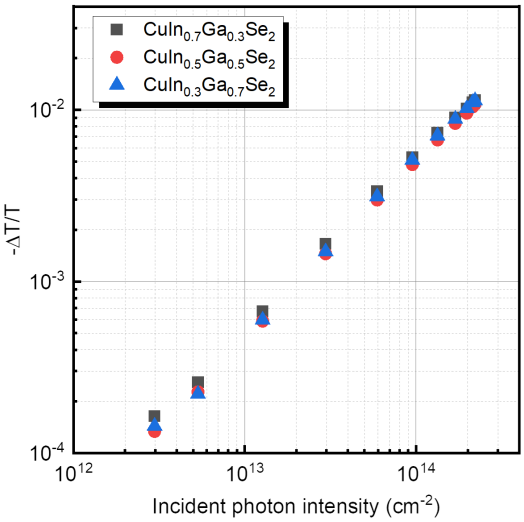

Figure 3.1: Maximum value of the transient transmittance as a function of the incoming photon density, showing the linear relationship between the two quantities.

3.3 Results and discussion

Figure 3.1 presents three panels comparing normalized TRTS dynamics for air/CIGS (green traces) and ZnO/CdS/CIGS samples red traces), as defined by the three analyzed Ga contents. The pump photons (800 nm wavelength and pulse duration of 45 fs at 1 kHz repetition rate), impinging on the samples from either the air or the ZnO/CdS window, selectively excite the CIGS layer (*i.e.*, the excitation wavelength is unable to produce direct band-to-band transitions in ZnO/CdS capping materials). The light intensity was adjusted according to the penetration depth in order to have the same photogenerated carrier density in all the samples ($\approx 1.7 \cdot 10^{18}\,\mathrm{cm}^{-3}$). As follows from Equation (3.1), $\dfrac{\Delta T}{T_{ref}}$ is directly proportional to the sample's photoconductivity $\Delta\sigma = e \cdot \Delta N \cdot \Delta\mu$ (where e is the

electron charge, ΔN is the photoinduced charge carrier density, and $\Delta\mu$ is the photoinduced electrical mobility), the resolved dynamics in Figure 3.1 might, in principle, reveal photoinduced changes in both carrier density or mobility as a function of time. Analysis of the THz frequency-resolved complex conductivity as a function of pump–probe delay demonstrates that mobility is barely affected upon pump–probe delay for each set of samples (*i.e.*, $\Delta\mu(t) = \mu$). As such, the monitored dynamics in each panel of Figure 3.1 are primarily revealing recombination kinetics in the samples (that is, $\Delta\sigma(t) = e \cdot \Delta N(t) \cdot \mu$). Provided that the electron effective mass is between 2 and 4 times lighter than the hole effective mass for Ga contents between 0 and 1,[62] we interpret our OPTP signal as describing predominantly electron dynamics. First, we compare the electron recombination kinetics for samples consisting of air/$CuIn_{1-x}Ga_xSe_2$ interfaces (green squares) as a function of Ga content. As evident from the plots in Figure 3.1, the electron dynamics for air/CIGS samples can be well described by a biexponential function with fast and slow decay time constants of $\tau_{\text{fast}} \approx 100\,\text{ps}$ and $\tau_{\text{slow}} \approx 1000\,\text{ps}$ (the origin for this biexponential deactivation path is discussed later). As the Ga content is increased, the overall recombination kinetics becomes faster (see green traces in Figure 3.1a-c). This result alone demonstrates that increasing Ga contents leads to enhanced recombination rates in the CIGS layers.

Interestingly, comparing air/CIGS kinetics with those obtained from ZnO/CdS/$CuIn_{1-x}Ga_xSe_2$ samples with high Ga contents ($x = 0.5$ and 0.7; red symbols in Figure 1b,c), reveals that charge carrier dynamics are barely affected by the presence of ZnO/CdS overlayers. That is, ZnO/CdS capping does not induce any measurable passivating effect on samples with bandgaps above 1.2 eV. This result demonstrates a negligible effect of the CdS buffer layer on inhibiting surface (or bulk) recombination in samples with a high Ga content. On the other hand, the sample with the lower Ga content ($x = 0.3$ and bandgap of $\approx 1.2\,\text{eV}$, the state-of-the-art composition), shows a clear change in recombination kinetics upon CdS treatment. The CdS treatment produces a 24% increase in amplitude at 900 ps after pump

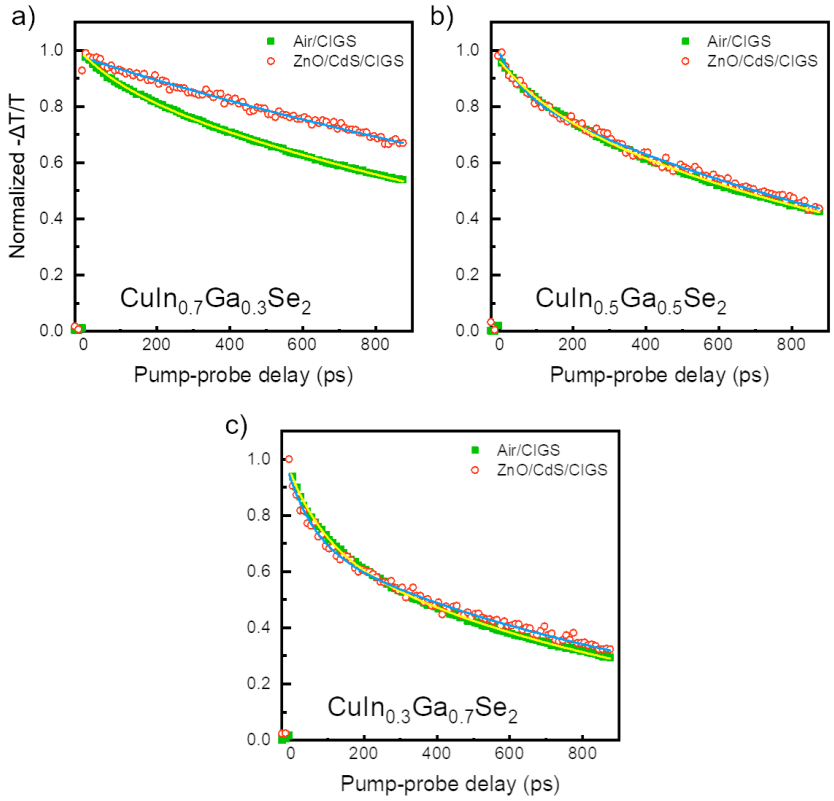

Figure 3.2: a-c) Normalized optical pump–THz probe dynamics on CIGS samples with Ga contents of $x = 0.3$ (a), $x = 0.5$ (b), and $x = 0.7$ (c). The green squares represent the decay for the air/CIGS samples, while the red open circles depict the transient signal for the ZnO/CdS/CIGS samples. The solid lines indicate the best biexponential fits to the data (single exponential for the low Ga ZnO/CdS/$CuIn_{0.7}Ga_{0.3}Se_2$ sample). In all cases, the photogenerated carrier density per pulse equals $1.7 \cdot 10^{18}\,\mathrm{cm}^{-3}$.

excitation that demonstrates unambiguously an improvement in carrier density (photocurrent) resulting from effective passivation of the CdS/CIGS interface. Notably, the CdS capping gives rise to the disappearance

of the fast decay component, leaving the dynamics single-exponential, defined only by the $\approx 1000\,\mathrm{ps}$ long-lived τ_{slow} component, also observed for the uncapped samples. Therefore, we can conclude that the fast component τ_{fast} is associated with trapping at the CdS/CIGS interface (*i.e.*, with interfacial recombination). Overall, the results shown in Figure 3.1 demonstrate that the passivating effect of the CdS treatment onto CIGS absorbers is Ga-dependent; being uniquely effective for the low Ga content sample. These observations correlate very well with the drop in efficiency observed in CIGS-based devices with high Ga contents In addition, OPTP dynamics for samples deposited onto soda-lime glass and fused silica are indistinguishable, revealing that the nature of the substrate employed in THz measurements and solar cell devices does not substantially alter the chemistry of the samples at the probed interface. To validate the conclusion that the surface recombination component is uniquely associated with the fast $\approx 100\,\mathrm{ps}$ component, we performed a fluence-dependent analysis of the samples. The intention was to deliberately saturate surface traps by photodoping. Figure 3.3a presents optical pump–THz probe traces as a function of incident photon density for the low-Ga sample exposed to air within the range of $3.0 \cdot 10^{12}$ to $2.2 \cdot 10^{14}\,\mathrm{photonscm}^{-2}$ per pulse (with estimated carrier densities in the range between $1.7 \cdot 10^{17}$ and $1.2 \cdot 10^{19}\,\mathrm{cm}^{-3}$, comparable with solar cell devices operating under 1 sun illumination). As it is evident from the plot, increasing the pump fluence for the low-Ga air/CIGS sample results in a reduction of the weight of the fast recombination component. For sufficiently high photon fluxes, the dynamics become single exponential and defined only by the long-lived $\approx 1000\,\mathrm{ps}$ component. The lifetimes and relative amplitudes obtained from biexponential fits to the data for the evolution of the fast and slow kinetic components as a function of photon flux are summarized in Figure 3.3b,c. The data reveal that τ_{slow} (linked to CIGS bulk recombination) is barely affected by fluence over the analyzed range of excitations. However, τ_{fast} (linked to surface recombination at the air/CIGS interface) becomes smaller in amplitude and that at elevated photon fluxes, increasingly

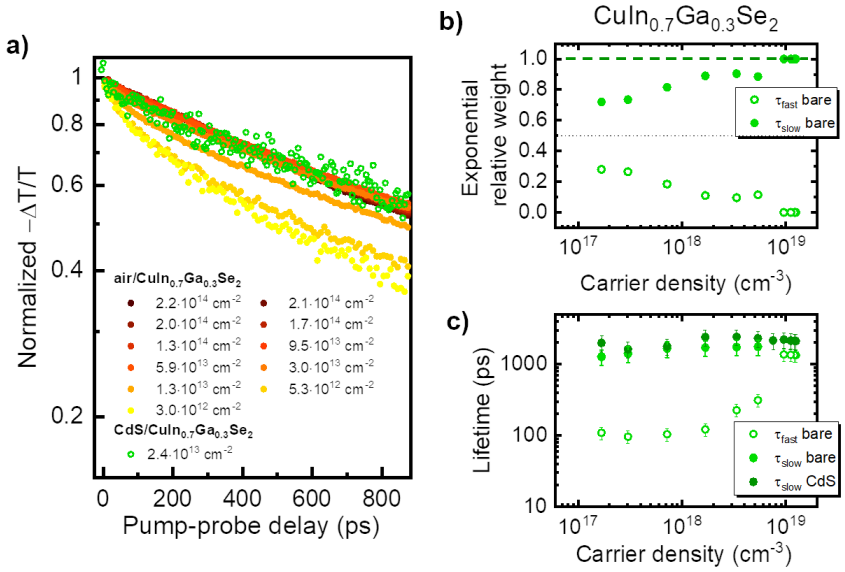

Figure 3.3: a) Comparison between charge dynamics in air/$CuIn_{0.7}Ga_{0.3}Se_2$ with increasing excitation density (solid dots) and $CuIn_{0.7}Ga_{0.3}Se_2$ (green open circles). b,c) The relative weight and lifetimes obtained from biexponential fits to the data as a function of photoinduced carrier density.

slower trapping timescales are obtained (consistent with the notion that that trapping rate is directly proportional to trap density).[63–65] Also, we observe that the carrier dynamics of the low Ga content for ZnO/CdS/CIGS samples at low fluences (open green dots in Figure 3.3a) correlate very well with those obtained for air/CIGS samples at high photon fluences, suggesting that photodoping reaches almost the same passivating effect as the CdS-capping. These observations confirm the assignment of the fast and slow trapping components to surface and bulk effects, respectively.

Finally, we performed fluence-dependent analysis for the high-Ga samples ($x = 0.5$ and $x = 0.7$ Ga contents). Quantitative analysis of the data, from biexponential fits (see Figure 3.4a,b), reveal, when compared

with the low-Ga sample (Figure 3.3c), a much weaker trap filling effect (affecting only the fast surface-related component) for the sample with Ga content of x = 0.5. On the other hand, no evidence is found for trap filling in the high-Ga sample ($x = 0.7$, Figure 3.4b), which presents almost invariant trapping time constants of ≈ 100 and ≈ 1000 ps for all the analyzed photon fluences corresponding to carrier densities ranging from $\approx 10 \cdot 10^{17}$ to $10 \cdot 10^{19}\,\mathrm{cm}^{-3}$. These results illustrate that the surface defect population for high-Ga samples is much larger than the maximum carrier density induced by the larger photon flux employed in this study ($\approx 10 \cdot 10^{19}\,\mathrm{cm}^{-3}$). The relative amplitudes for the slow and fast components obtained from biexponential fits to the data are presented in Figure 3.4c,d. Notably, the data reveal that, at elevated charge densities, both high Ga content samples ($x = 0.5$ and $x = 0.7$) show an increase in the weight associated with the component ascribed to surface recombination, suggesting an increase in defect population at the CdS/CIGS interface with photon flux. We interpret this observation with the promotion of metastable light-induced acceptors for high-Ga alloys.[41, 52] These metastable traps have been associated with the formation of divacancies ($V_{Se}-V_{Cu}$) at the CdS/CIGS interfaces under "red illumination" (*i.e.*, light not absorbed by the window/buffer layer as in our experimental conditions) and are expected to be dominant for high Ga content CIGS absorbers. The Ga content-dependent promotion of interfacial traps induced by light at the CdS/CIGS surface underlines even more the main conclusion of this paper: Ga-dependent surface recombination, rather than bulk, determines photoconversion efficiency in CIGS samples as a function of Ga content.

3.4 Concluding remarks

In conclusion, we report the interplay between surface recombination and CIGS stoichiometry. We demonstrate that surface recombination is Ga content-dependent for CIGS absorbers, at both air/CIGS and ZnO/CdS/CIGS interfaces; being increasingly dominant for samples

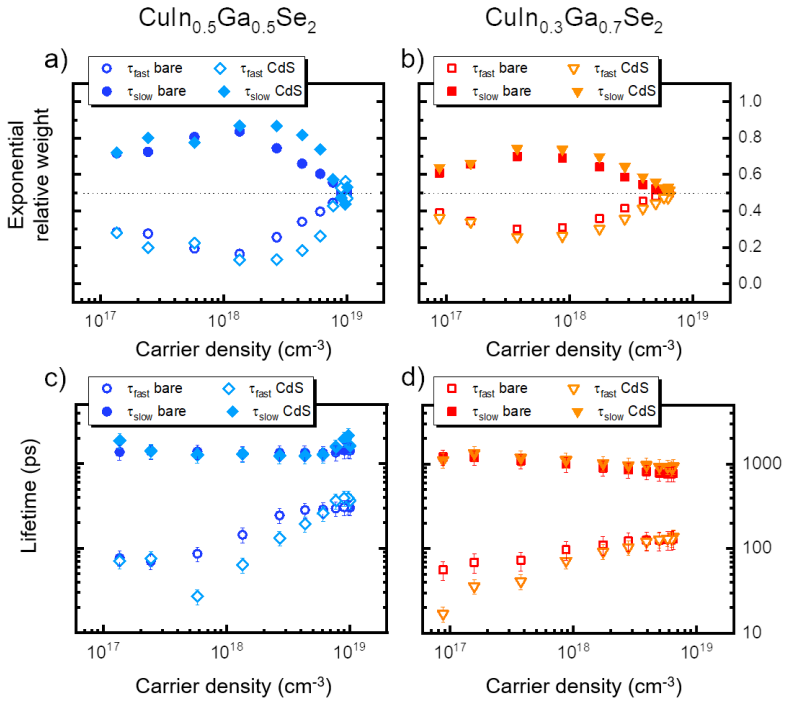

Figure 3.4: a,b) Relative weight of the time constants as a function of the charge carriers photogenerated in the system according to the biexponential fit for $CuIn_{0.5}Ga_{0.5}Se_2$ (a) and $CuIn_{0.3}Ga_{0.7}Se_2$ (b). c,d) The respective lifetime extracted for the two samples.

with larger Ga contents and therefore larger bandgaps. Furthermore, we demonstrate that CdS capping is only effective in removing surface recombination for the low-Ga samples. Our data further reveal the formation of light-induced acceptors at the CdS/CIGS interface for high-Ga samples. Altogether, our results correlate well with the observed Ga-dependent efficiency trend in device performance and demonstrate that the drop of efficiency in cells made with larger bandgaps can be attributed, at least partially, to surface recombination at the CdS/CIGS interface. Note that the relative band alignment at the CdS/CIGS interface as a function of

Ga content might impose as well a V_{OC} deficit in solar cells. Interfacial engineering could, therefore, prove a way forward for further increasing the efficiency of CdS/CIGS-based devices.[66]

3.5 Additional information

Fluence dependence with high Gallium content

The behavior of high-Gallium-CIGS alloys under increasing light intensity differs substantially from the $CuIn_{0.7}Ga_{0.3}Se_2$ shown in Figure 3.3. In the latter case, we assign the observed behaviour to a slowing down of carrier recombination, while for $CuIn_{0.5}Ga_{0.5}Se_2$ and $CuIn_{0.3}Ga_{0.7}Se_2$, we observe the opposite trend. This feature is commonly associated with the enhancement of bi-molecular recombination probability over the trap-assisted path. Another possibility is the formation of a new type of metastable defect, *e.g.*, a Selenium-Copper vacancy complex($V_{Se}-V_{Cu}$), which becomes energetically favourable for a high Ga-concentration, as suggested by Lany and coworkers.[52] For every photon density employed, in the range between $2.97 \cdot 10^{12}$ and $2.21 \cdot 10^{14}\,cm^{-2}$, the deposition of the CdS layer does not have any apparent effect on the carrier dynamics. The absence of any measurable effect following the surface treatment is again proof that CdS is not passivating the surface of wide gap CIGS.

Frequency resolved complex conductivity

In this chapter, we assume that the mobility remains constant during the observed photoconductivity decay. The validity of this former statement arises from the analysis of frequency-resolved conductivity spectra. We extracted the normalized conductivity spectra at different pump-probe delays (Figure 3.6, probing at 100 and 800 ps after the photoexcitation).

The data have been fitted with the Drude-Smith model as reported in Equation (1.13) and, according to the best fits, the scattering times are reported in Table 3.1.

The scattering rate τ is rather constant with time after photoexcitation; only for the low Ga-containing sample, an increase in mobility at long pump-probe delays is observed, which we assigned to electron transfer into

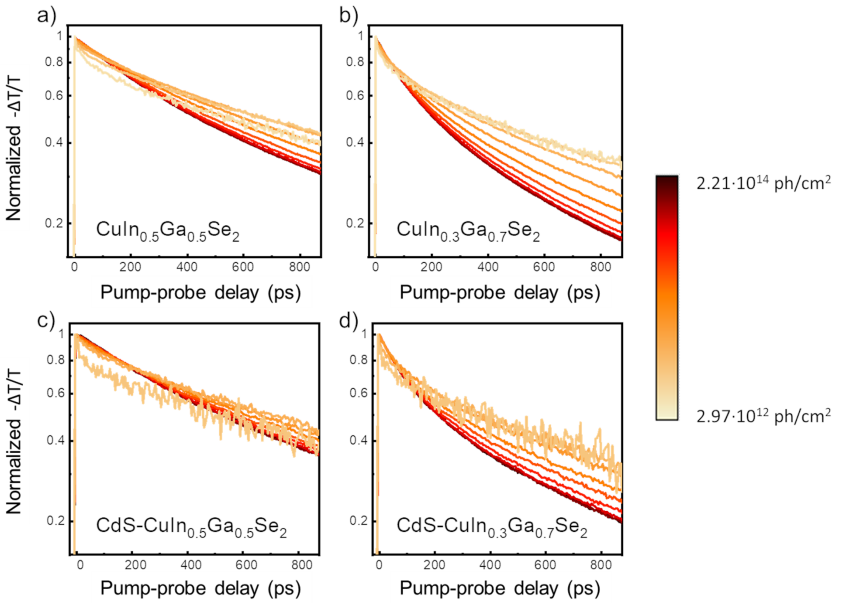

Figure 3.5: Time resolved transient transmittance in $CuIn_{0.5}Ga_{0.5}Se_2$ (a), $CuIn_{0.5}Ga_{0.5}Se_2$ (b), $CdS-CuIn_{0.5}Ga_{0.5}Se_2$ (c) and $CdS-CuIn_{0.3}Ga_{0.7}Se_2$ (d) as a function of the incident photon density.

Table 3.1: Scattering times from the best fit to the Drude-Smith model for the three CdS/CIGS sample, measured at 100 and 800 ps after the photoexcitation with the 800 nm laser beam. The reported values have to be intended with an error of 5 fs.

Sample	τ at 100 ps	τ at 800 ps
$CdS-CuIn_{0.7}Ga_{0.3}Se_2$	47 fs	65 fs
$CdS-CuIn_{0.5}Ga_{0.5}Se_2$	55 fs	64 fs
$CdS-CuIn_{0.3}Ga_{0.7}Se_2$	35 fs	38 fs

the higher-mobility ZnO. The fact that this is only observed for the low-Ga samples is consistent with the notion of having a kinetic competition

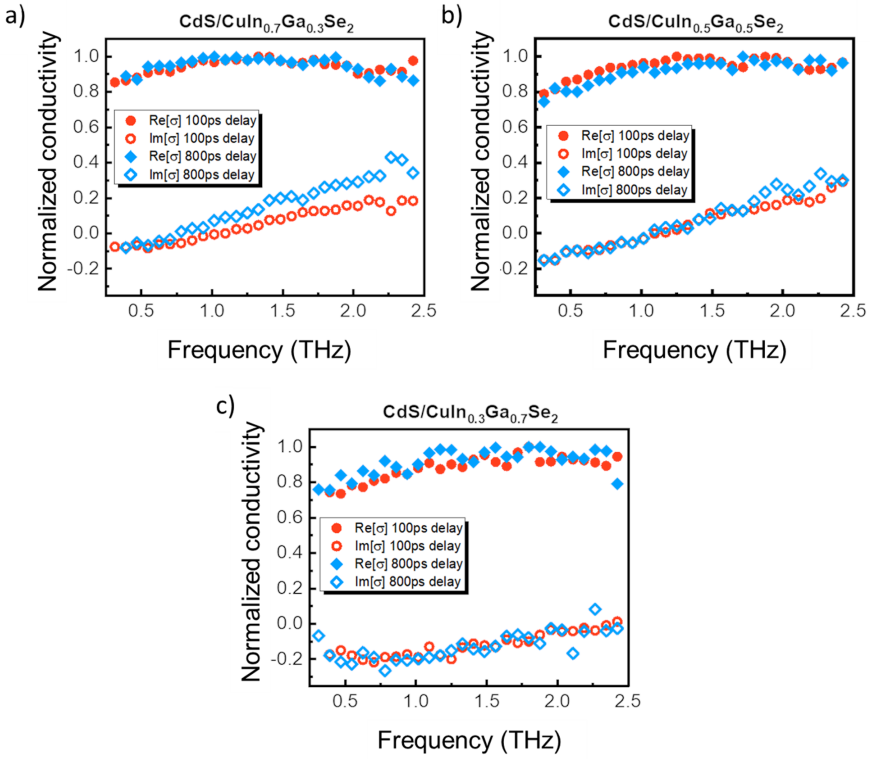

Figure 3.6: Normalized frequency-resolved conductivity collected at 100 ps (red circles) and 800 ps after photoexcitation (blue diamonds). Solid lines represent best fits to the Drude-Smith model.

between injection towards the ZnO and interfacial recombination at the CdS/CIGS interface, the latter being maximized in high Ga samples.

Comparison between fused silica and Soda-Lime glass (SLG) substrates

To investigate the eventual role of the substrate on the observed kinetics in more detail, we prepared a set of samples consisting of CIGS samples

with Ga contents of ($x = 0.3$) and ($x = 0.5$) on both fused silica and soda-lime glass (SLG). The samples were measured by optical pump THz probe under similar excitation conditions (800 nm, 50 µJ/cm^2).

The measurements on SLG substrates are clearly noisier owing to the lower transmission of the THz probe through the SLG substrate, while fused silica is transparent in our probing window dictated by the ZnTe emission profile. As shown in Figure 3.7 the obtained kinetics for both Ga contents are identical and independent of the employed substrate. Clearly, the details of the substrate do not alter the kinetics, leaving the conclusions of this work intact.

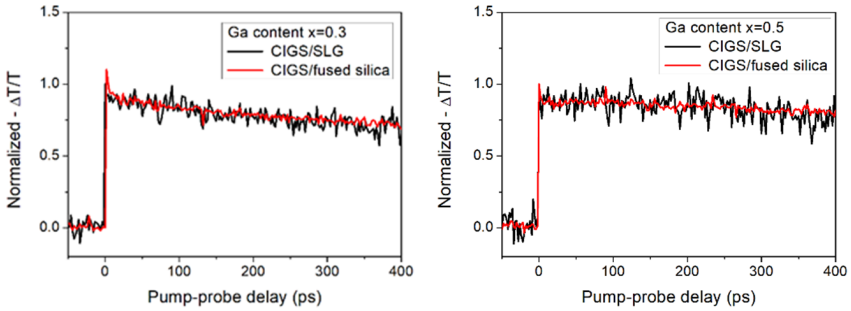

Figure 3.7: OPTP dynamics for CIGS samples with Ga contents of $x = 0.3$ and $x = 0.5$ (left and right panels) deposited on fused silica and soda-lime glass (red and black traces respectively).

Chapter 4

Charge transport in doped polyaniline

4.1 Introduction

Conductive polymers are attractive electroactive materials for organic electronics since their conductivity can be tuned, reversibly, more than thirteen orders of magnitude under chemical doping and de-doping cycles.[67, 68] The enhancement of the conductivity in these materials comes from the generation of extended states in doped molecules, states that are generally attributed to the creation of quasiparticles (e.g. solitons and polarons), a view supported by optical spectroscopy and magnetic measurements.[69, 70] The charge transport in polymers is most often described as a thermally activated process, a hopping mechanism linked with localized charge carriers. Thermally activated transport is enabled by charge carrier motion along the conjugated backbone (*i.e.* intra-chain, dominating at higher frequencies), and inter-chain processes between conductive domains dominating the long-range transport macroscopically (*i.e.* towards the DC limit). Within this picture, most work over the past decades has been devoted to engineering band-like charge transport in conducting polymers. To achieve that, both inter- and intra-molecular overlap of frontier orbitals is required to form a delocalized electronic band.[71, 72] With this target in mind, many efforts have aimed at exploiting methods

for improving the long-range ordering/crystallinity of conducting polymers, thereby hoping to maximize charge carrier delocalization within the polymer backbone.[73–76] Indeed, state-of-the-art results in terms of conductivity and mobility figures in conductive polymers are often linked with highly crystalline samples.[77, 78]

In this work, we prepare highly ordered thin films of quasi two-dimensional polyaniline (q2D-PANI) with phytic acid (PA) as a dopant during surfactant monolayer assisted interfacial synthesis (SMAIS).[78] This singular dopant does have six phosphate groups that could release more than one proton per molecule; furthermore, PA is expected to enable the coordination of multiple aniline sites, acting then as a bridge between adjacent conductive domains to improve long-range transport in the samples.[79]

Following SMAIS synthesis, we observed that PA concentrations as low as 3 mM in PANI produced an optical density at 800 nm, generally assigned to the polaron band, which is commensurate to the one obtained in q2D-PANI samples doped with up to 1 M HCl. Moreover, structural and compositional characterization for the PA doped PANI films (PA-PANI) revealed a reduced crystallinity when compared with HCl-doped PANI,[78] indicating that the PA dopant is perturbative towards crystal structure. Increasing the PA dopant concentration from 3 mM to 75 mM, the PANI film becomes increasingly amorphous. To study the impact of PA doping on the sample's conductivity, we characterized the frequency-resolved complex conductivity in the THz region by time-resolved THz spectroscopy (TRTS). The results demonstrated that, remarkably, Drude-like band conduction characterized charge transport in all samples independently of doping content, and most importantly, independently of their degree of crystallinity. Even the most-doped, least-crystalline samples revealed the highest charge carrier scattering rates and corresponding the highest mobility ($1\,\mathrm{cm^2V^{-1}s^{-1}}$) and conductivity ($93\,\mathrm{Scm^{-1}}$). This counter-intuitive result is rationalized by PA promoting cross-linking between conductive domains in PA-PANI, and aligns with the findings of previous reports

where high mobility have been observed in highly disordered or even amorphous samples.[80] Finally, temperature-dependent experiments reveal a scattering rate barely affected by temperature, indicating that impurity scattering is the limiting mechanism in the mobility for the PA doped PANI samples.

4.2 Sample synthesis and characterization

The synthesis procedure for PA-PANI by SMAIS is similar to the one described previously and summarized in Figure 4.1. In brief, a surfactant (sodium oleyl sulfate, SOS) monolayer was prepared on the water surface in a glass well (50 mL, $\varnothing = 6$ cm), followed by the addition of aniline monomers (11.5 µL in 1 mL water) in the water subphase. The glass well was then covered with a petri dish and kept under 1 °C. After 24 h, hydrochloric acid (HCl, 0.02 M), phytic acid (PA, 3 −75 mM), and ammonium persulfate (APS, 2.5 mg in 1 mL water) were successively injected into the water subphase to trigger the polymerization. After a certain polymerization time (12-48 h), a uniform and continuous polymer film of a dark green color appears on the water surface.

The resultant PA-PANI film on water is robust enough to be transferred intact onto different substrates for morphological and structural characterizations. For instance, a ≈ 60 nm thick PA-PANI film could suspend over the large holes of $\approx 400\,\mu m^2$ of a TEM grid (Figure 4.2a). Under the optical microscope, the PA3-PANI (prepared in 3 mM PA solution) transferred onto SiO_2/Si is homogeneous, and the edges of the film are clearly visible (Figure 4.2b). Atomic force microscopy (AFM) measurement at film edges reveals an average thickness of 59 ± 3 nm and a low surface roughness. after 12 h of polymerization (Figure 4.2c). In all the analyses carried out for this work, the reaction time for the preparation of the PA-PANI films was set as 12 hours.

X-ray photoelectron spectroscopy (XPS) reveals that the PA3-PANI films contain carbon, nitrogen, phosphorus, chlorine, and oxygen in a ratio

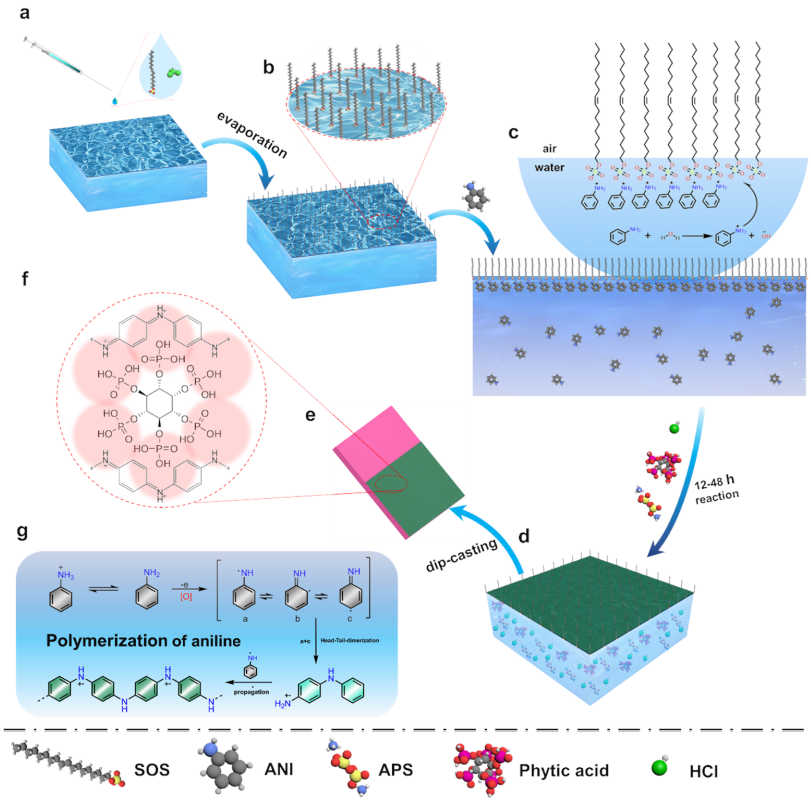

Figure 4.1: Schematic illustration of the synthesis procedure for PA-PANI. a) Addition of the SOS surfactant solution on water surface. b) Formation of surfactant monolayer after the evaporation of solvent. c) Addition of the aniline (ANI) monomer into the water sub-phase. d) Oxidative polymerization triggered by APS, phytic acid, and HCl. e) Transfer of the film onto the substrate. f) Scheme of the proposed arrangement between phytic acid and the polyaniline chains. g) Polymerization reaction mechanism of aniline monomers.

of 56.4%, 6.74%, 6.32%, 0.46%, and 30.09% (Figure 4.2d), respectively. Two prominent peaks of N1s at 401.9 eV and 399.8 eV can be attributed to two types of nitrogen ($-NH^+-$ and $=NH^-$) in PA3-PANI (Figure 4.2e). The peak at 134.1 eV belongs to the PO_4H_2 moiety of PA. The three

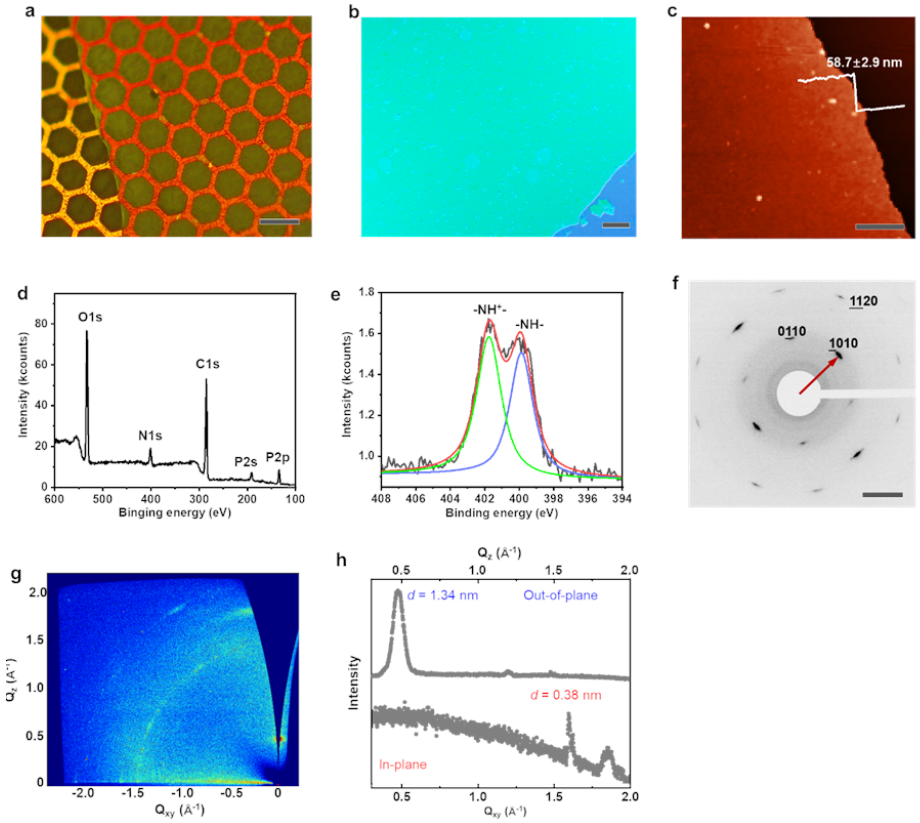

Figure 4.2: Optical microscopy images of PA3-PANI film (a) suspended over a copper grid and (b) transferred onto SiO2/Si wafer. (c) Atomic force microscopy (AFM) image and thickness value of PA3-PANI after the 12-h reaction. (d) XPS spectrum and (e) high-resolution N1s. The fitting in (e) was performed with a set of Voigt peaks. (f) SAED pattern of PA3-PANI along the [0001] axis, the [010] and [010] reflections are at 3.06 nm-1. (g) GIWAXS pattern of PA3-PANI on a Si wafer. (h) In-plane and out-of-plane projections from (g). Scale bars: (a-b) 20 µm; (c) 2 µm; (f) 2 nm^{-1}.

peaks of C1s signal can be assigned to C1s of C−C at 284.8 eV, C=C at 284.8 eV, C−N at 286.5 eV, and C−N at 288.2 eV, respectively. Fourier

transform infrared spectroscopy of PA3-PANI shows the characteristic bands of quinoid and benzenoid rings at 1575 and 1498 cm^{-1}. Bands at 1302 and 1242 cm^{-1} arise from the C–N stretching of the secondary aromatic amine and C–N stretching vibration in the polaron structures, respectively. Meanwhile, the band at 1647 cm^{-1} is attributed to the stretching frequencies of the P=O groups.

The UV-Vis spectra of PA3-PANI film reveals a similar absorbance with that of HCl-doped PANI (Figure 4.3).[67,81,82] The feature at 400 nm (3 eV) is generally assigned to the $\pi - \pi^*$ transition of the benzenoid ring.[81] On the low energy side, the asymmetric absorption band peaking around 800 nm (1.5 eV) is attributed to the transition from the π level to a polaron state, which is generally considered the fingerprint of the protonated, conductive emeraldine salt.[69,70,81] However, in comparison to the 1 M HCl doped q2D-PANI, the 3 mM PA doped PANI polaron band seems to extend towards the IR, which can be an indicator of more delocalized conductive states.[82] Furthermore, it is remarkable how the polaron band for 3 mM PA doped samples matches in absorption strength the one made by 1 M HCl doping, a possible consequence of PA promoting more efficient doping of the PANI chains per dopant molecule.

Figure 4.2f shows the representative selected area electron diffraction (SAED) patterns of PA3-PANI along [001] axis, which reveals a hexagonal lattice with the [1010] and [0110] reflections at 2.65 nm^{-1}, corresponding to in-plane spacing of $a = b = 0.38$ nm. Grazing-incidence wide-angle X-ray scattering (GIWAXS) shows that the PA3-PANI film is polycrystalline at a microscopic scale (Figure 4.2g), and the out-of-plane distance $c = 0.37$ nm. As such, the molecular structure of the PA3-PANI can be depicted as shown in Figure 4.1f, where the adjacent PANI chains along the in-plane direction are cross-linked by the phosphate groups of PA dopant. Note that the same SMAIS protocol employed for developing HCl doped PANI samples led to highly ordered, quasi two-dimensional samples with square symmetry.[78] That is, despite following almost the same synthetic approach, the addition of PA in PANI samples was perturbative upon the crystallinity of the final

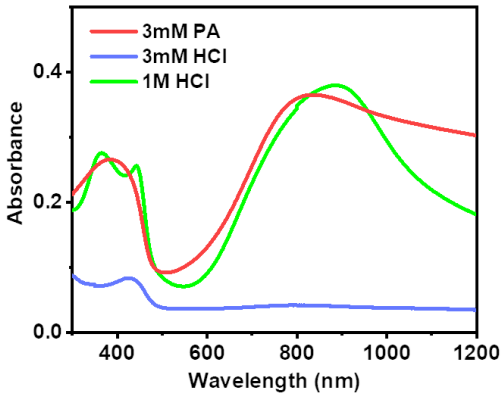

Figure 4.3: Absorption spectra of PANI films doped by 3 mM PA (red), 3 mM HCl (blue), and 1 M HCl (green), respectively

film.

After the preliminary characterization that confirms the inclusion of PA acid molecules in the ordered structure of PA3-PANI, we characterized the effect of doping content on the samples. Figure 4.4a shows the absorbance spectrum of PA-PANI thin film samples doped with 3, 15, and 75 mM of PA. The amplitude of the absorption band peaking around 800 nm increases significantly with the increase of added concentrations of PA. XPS spectra in Figure 4.4b show that the element ratios of P:N in the resultant PA-PANI films are 0.46 (3 mM), 0.64 (15 mM), and 0.94 (75 mM), respectively. In addition, high-resolution N1s core level spectra show that the contents of doped/charged N in PA-PANI films are 53.80%, 59.48%, and 83.44%, respectively (Figure 4.4c). These results demonstrate that the doping level of PA-PANI can be controlled by increasing PA concentrations during the SMAIS synthesis. The undoped sample (by 1 M NH_4OH) is characterized by an absorption band centered at ≈650 nm (≈1.9 eV, Fig. S6), which can be attributed to the HOMO-LUMO transition of the emeraldine base,

a non-conductive form of polyaniline.[28] Interestingly, GIWAXS results show that the increase of PA content leads to a rapid decrease in the degree of crystallinity of PA doped PANI films (Figure 4.4d-f), which we tentatively attribute to a large steric effect of PA molecules as well as the strong interaction between PA and PANI chains.

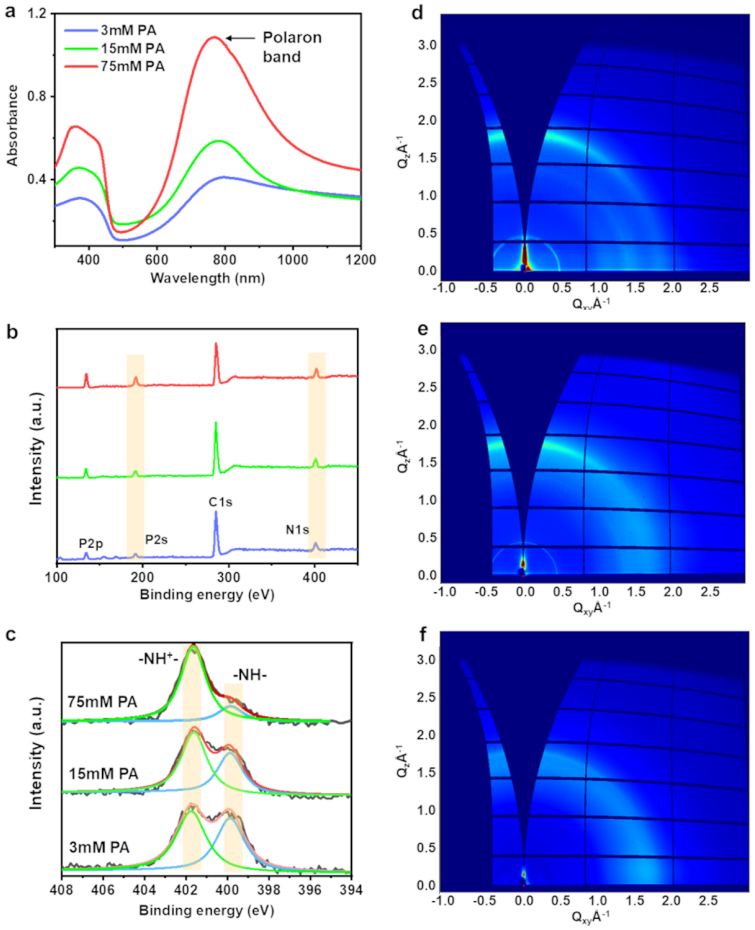

Figure 4.4: (a) Absorption spectra of PA-PANI prepared with 3 mM (blue), 15 mM (green) and 75 mM (red) PA, respectively. (b) XPS survey spectra of the samples in (a), from which the element ratio of P:N in PA-PANI films can be calculated (c) high-resolution N1s core level spectra of the PA-PANIs in (a), from which the ratios of doped/charged N in PA-PANI can be calculated. (d-f) The GIWAXS pattern of the 3PA, 15PA and 75PA-PANI films.

4.3 Charge transport analysis

We photo-excite the sample with a 50 fs laser pulse centered at 800 nm. After the absorption of the pump beam, a THz probe pulse interrogates the photoconductivity of the sample in a non-invasive way. The THz pulse is generated by the same laser system via optical rectification in a ZnTe crystal providing a bandwidth of 0.3-2.5 THz.[33, 34, 83] By definition, we can express the photoconductivity in the sample as $\Delta\sigma = -e\Delta N\mu$, where e is the electron charge, ΔN the variation in charge carrier density induced by the pump, and μ is the sample's mobility. Following an optical pump-THz probe scheme (OPTP), we can obtain sub-ps dynamics linked with photoinduced changes for the real and imaginary components of the conductivity. In Figure 4.5a, we plot the real part of conductivity as a function of pump-probe delay for the set of PA doped samples shown in Figure 4.4 (all samples are ≈100 nm in thickness, photon excitation intensity of $4.4 \cdot 10^{19}$ photons/m^2 at 1.55 eV). Under the employed experimental conditions, we find that all PA doped samples are characterized by an abrupt rise in photoconductivity induced by the pump, which is followed by a decay that can be phenomenologically modeled with a double exponential function. The best fit to the data returns lifetime values of $t_1 = 0.8 \pm 0.1$ ps and $t_2 = 5 \pm 2$ ps for the fast and slow components, respectively. The obtained dynamics resemble those reported previously in THz studies in other conventional organic semiconducting polymers,[84, 85] where the fast initial decay is generally assigned to charge trapping or to the condensation of quasi-free charges that thermalize into bound, neutral excitons. In both scenarios, the fast decay represents pump-induced species that do not contribute to the photoconductivity beyond 1 ps. On the other hand, the long-lived 50 ps component strongly suggests that a significant fraction of photoinduced species is conductive, that is, they are not falling immediately into bound states. Note that this holds independently of sample crystallinity.

To further understand the nature of the observed charge dynamics

and investigate whether excitons are present in the samples beyond 1 ps, we analyze the dependence of the photoconductivity as a function of impinging photon flux for the 75 mM doped PANI sample. Figure 4.5b presents a summary of the OPTP data obtained as a function of photon intensity (in the range between $\approx 6 \cdot 10^{17}$ and $6 \cdot 10^{19}$ photons/m^2). The negative signals represent the dynamics for the imaginary component of the pump-induced conductivity, monitored by following pump-induced phase shifts in the THz waveform as a function of time. Changes in the phase of the propagating THz probe might be indicative of polarizable neutral excitons in the samples. If excitons were present, a long-lived imaginary conductivity component would be obtained beyond the initial fast real conductivity decay. This, of course, is true only if the excitons have non-negligible polarizability in the THz frequency region, i.e. they are loosely bound. As evident from Figure 4.5b, imaginary dynamics are defined by only an ultrafast decay that completely vanishes within 2 ps, independently of adopted fluence. This behaviour is consistent with a lack of polarizable excitons in the samples. The observed timescale of the imaginary conductivity deactivation matches fairly well the short live component resolved for the real conductivity in the samples as a function of time and can be tentatively interpreted in terms of free photoexcited species that undergo ultrafast charge trapping.[86] On the other hand, the long-lived real conductivity should be attributed to a residual population of delocalized free charge carriers in the sample. Fluence dependence analysis for the real conductivity component in Figure 4.5b also shows an onset for the appearance of the long-lived component above an excitation density of $\approx 10 \cdot 10^{19}$ photons/m^2, which can give an indication about the number of active traps in the material, that is, the emergence of the signal could be linked with trap filling effects.

The previous analysis on carrier dynamics inferred from TRTS strongly indicates that free delocalized charge carriers are the main products in the samples for excitations above $\approx 10 \cdot 10^{19}$ photons/m^2 and timescales above ≈ 2 ps. We can corroborate whether these findings are correct by

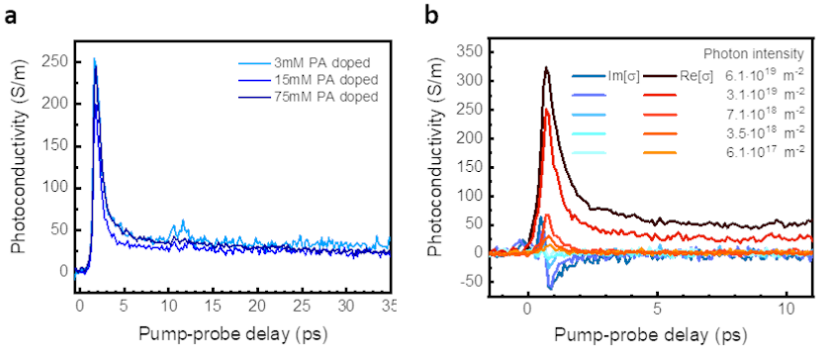

Figure 4.5: (a) photoconductivity from optical pump-THz probe on 3 , 15 and 75 mM PA doped PANI sample (blue lines) under a photon intensity of $4.4 \cdot 10^{19}\,\mathrm{m}^{-2}$. (b) Real (positive red traces) and imaginary (negative blue traces) parts of the time-resolved photoconductivity in 75 mM doped PANI as a function of excitation density.

addressing the nature of charge transport in the samples, this can be accomplished by analyzing the frequency-resolved complex conductivity of the signals in the range between 0.3 and 2.3 THz, limited by the output of our ZnTe emitter. In Figure 4.6 we present the conductivity spectra of all PA-PANI samples analyzed in this work, obtained by the Fourier transform of the time domain transmitted pulses. In these experiments, the excitation fluence equals $4.4 \cdot 10^{19}\,\mathrm{m}^{-2}$; conductivity traces were collected 10 ps after the photoexcitation (for data collected at the peak conductivity, see SI). Independently of the doping content, we resolved a decreasing real and increasing imaginary conductivity component with frequency within the probed THz region. All traces can be fairly well described by the Drude model (1.11). The Drude model is sufficient for all doping concentrations to explain the data. As such, we can conclude that the long-lived signals in OPTP dynamics refer unambiguously to free, delocalized charge carriers populating PA-doped PANI samples. It is worth mentioning here that Lee et al. have previously reported band-like Drude-like behavior in highly

crystalline PANI samples doped with camphor sulphonic acid.[77] In that case, they derived the real conductivity from Kramers-Kronig analysis on reflectivity spectra, in a frequency range limited above $500\,\mathrm{cm}^{-1}$ ($>$ 15 THz). The traces shown in Figure fig:pani2d reveal Drude responses from fits to the complex-valued conductivity and for frequencies as low as $10\,\mathrm{cm}^{-1}$ (0.3 THz). This allows us to fully rule out an eventual drop for the conductivity towards the DC limit, a signature for charge carrier localization.[5]

From the best fit of our data to Eq.(1.11), we can estimate a scattering time $\tau < 10$ fs for the samples doped by 3 and 15 mM PA, and a τ of about 29 ± 3 fs for the 75 mM PA doped sample. This observation reveals that the mobility of the samples is affected by doping content within the analyzed range. That is, doping affects not only the charge carrier density available for conduction but also their mobility. In previous reports scattering rates of 22 and 27 fs were reported in state-of-the-art PANI samples doped by camphor sulphonic acid.[80,87] Interestingly, we obtain the longer carrier scattering time for the sample that presents the lowest degree of crystallinity. While these observations may seem counterintuitive, they can be rationalized by considering that structural order and energetic order are not necessarily unequivocally correlated. Note that state-of-the-art mobilities up to $\approx 1\,\mathrm{cm}^2\mathrm{V}^{-1}\mathrm{s}^{-1}$ have been recently reported also in materials displaying low crystallinity or even, in some cases, of amorphous nature. For example, within these reports, high mobilities have been attributed to a network of tie chains providing interconnecting transport pathways between conducting domains.[72,80,88] This crosslinking effect might be suppressed in highly ordered structures. Furthermore, if a specific dopant is perturbative towards morphology (*e.g.* affects polymer chain planarity), it might have a beneficial role towards intrachain conductivity, provided that torsional effects along the backbone are well known to produce localized states.[89,90]

The scattering time, together with the effective mass, is the quantity that determines the electrical mobility following the relation $\mu = \dfrac{e\tau}{m^*}$.

According to most of the literature, there are two scenarios that have been linked with Drude-like responses in PANI samples, the presence of free band-like charge carriers or polarons,[77,91,92] the main difference regarding mobility estimates between both scenarios resides on the assumed effective mass for the populating charge carriers. Note that their spectral response in the THz region is not easily distinguishable.[93] If we assume that polarons (rather than free electrons) are the conductive species that are linked to the monitored Drude responses, we can estimate the mobility of the samples as $0.91 \pm 0.09\,\mathrm{cm^2V^{-1}s^{-1}}$ (or $30 \pm 3\,\mathrm{cm^2V^{-1}s^{-1}}$), where an effective mass of $M_{pol} = 56m_e$ is considered for polarons,[91] (alternatively, $m^* \approx 1.7m_e$ for free electrons).[77]

4.4 Temperature analysis

To better understand the nature of the transport in the PA-PANI samples, we performed a temperature-dependent TRTS analysis. 4.7, shows the impact of temperature on the time-resolved real part of the conductivity. The data reveal an increase in the monitored photoconductivity as the sample temperature is reduced from 290 to 77 K. This is exceptional behaviour for conductive polymers that usually exhibit thermally activated transport.[94] In Figure 6b, we present the frequency-resolved conductivity for the upper and lower limit tested temperatures for a 75 mM doped PA-PANI sample. For cooling the sample, it must be contained in a cryostat under vacuum. Under vacuum, that the Drude response is modified to a Drude-Smith (DS) response,[33] possibly from degassing the sample. The DS model accounts for Drude-like free carriers, which experience some degree of preferential backscattering (see SI for further details). In any case, the data in Figure 4.7 reveals that the conductivity of the sample improves with decreasing temperature, also in the DC limit (when $\omega \to 0$). The frequency-resolved complex conductivity spectra collected at every temperature show a clear free-carrier response. From fits to the DS model (solid and dashed lines in Fig.6b), we can obtain the variation of scattering

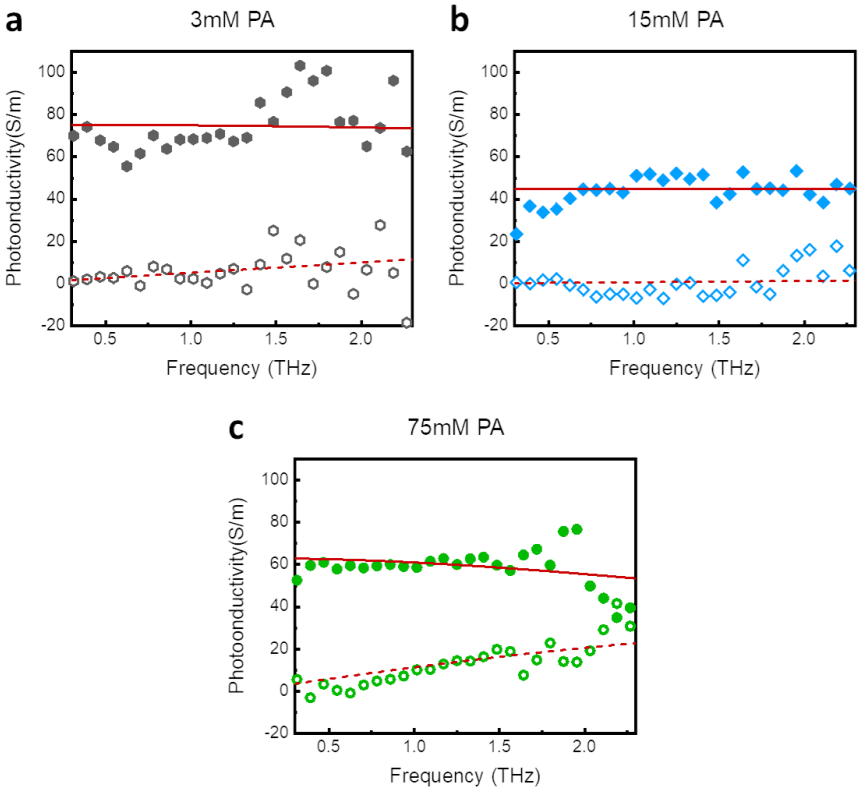

Figure 4.6: Frequency resolved photoconductivity of PA-PANI doped by 3 mM (a), 15 mM (b) and 75 mM (c) of phytic acid, measured 10 ps after photoexcitation. Full and empty symbols denote the real and the imaginary parts of the complex photoconductivity, respectively. Red solid and dashed lines represent the best fit to the data, according to the Drude model.

rate and plasma frequency as a function of temperature and then try to understand the origin for the unexpected increase in conductivity at reduced temperatures. Figure 6c summarizes the parameters obtained from the DS fits for two different samples of PA-PANI doped with 75 mM. The data reveals that the scattering rate is barely dependent on temperature,

an observation that suggests impurity scattering as a limiting factor for the charge carrier mobility.[95] Furthermore, the plasma frequency increases by approximately a factor of 2 from 290 K to 77 K. The increase in plasma frequency seems to explain alone the observed increase in conductivity at lower temperatures. An increase in plasma frequency ($\omega_p = \sqrt{\frac{N^2 e}{m^* \varepsilon_0}}$) could be rationalized with either an increase in photoinduced carrier density (N, where $N = \xi \cdot A \cdot N_{hv}$, where A refers to the fraction of absorbed photons and ξ is the photon to free carrier yield) or a reduction in free carrier effective mass. Provided that the amount of absorbed photons N_{hv} does not change with temperature (Figure 4.10), we speculate that an enhanced yield could be related with trap filling effects induced by a T-dependence of the background doping. Alternatively, a decrease in effective mass by reducing T has been suggested theoretically as a fingerprint of weak *e-ph* coupling in rubrene crystals displaying band-like transport signatures.[96, 97] At this stage, we are unable to conclude the dominant mechanism but, in any case, these observables do not alter the main conclusion derived from the T dependent analysis: impurity scattering limits free charge carrier motion in the samples. An observable which seems reasonable taking into account the non-crystalline nature of the analyzed samples.

4.5 Concluding remarks

We investigated the charge transport properties of polyaniline thin films achieved by SMAIS doped with a phytic acid dopant. Structural and elemental analysis confirms the inclusion of PA in the thin films and the progressive loss of crystallinity as the PA doping content is increased. Independently of doping content, the frequency-resolved complex conductivity spectra can be explained by the Drude model, revealing band-like transport in the samples. We found enhanced charge carrier mobilities for higher doping, despite the samples being notably less crystalline. This

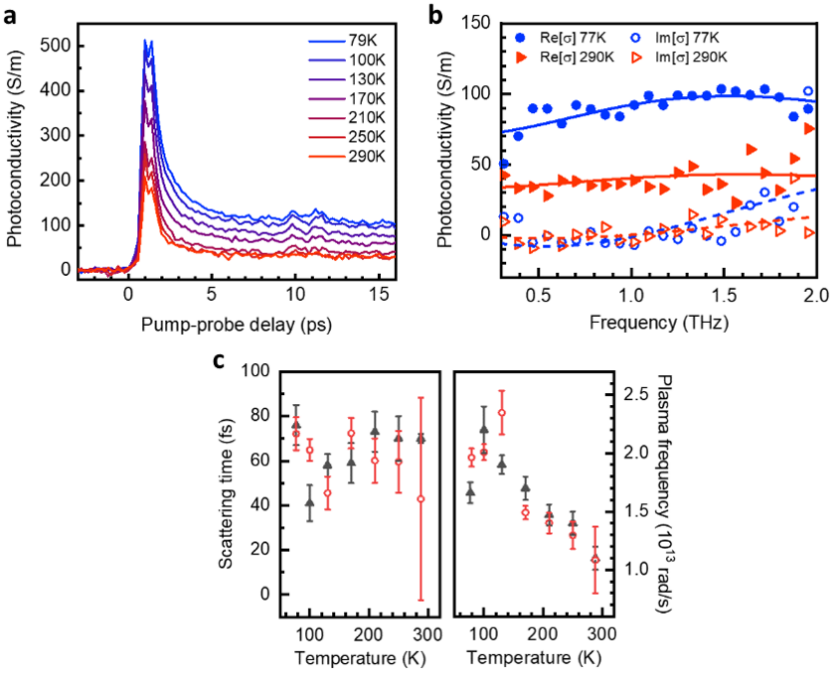

Figure 4.7: (a)Time-resolved photoconductivity as a function of temperature. (b) Complex-valued photoconductivity spectra at 77 K (blue circles) and 290 K(red triangles); solid lines are the real and imaginary components from Drude-smith fits. (c) Scattering times (left) and plasma frequencies (right) obtained from Drude-Smith analysis as a function of temperature for two sets of samples.

anti-correlation between conductivity and the degree of order in the samples indicates that while PA seems to promote structural disorder, it does increase energetic order, *e.g.* by enabling long-range charge transport between adjacent conductive domains. Finally, the temperature-dependent conductivity does not show any sign of thermally activated charge transport, in line with the notion of band-like conduction and loosely bound charge carriers.

4.6 Additional information

Drude-Smith analysis

We report here as follows the complete data relative to the frequency resolved photoconductivity as a function of temperature.

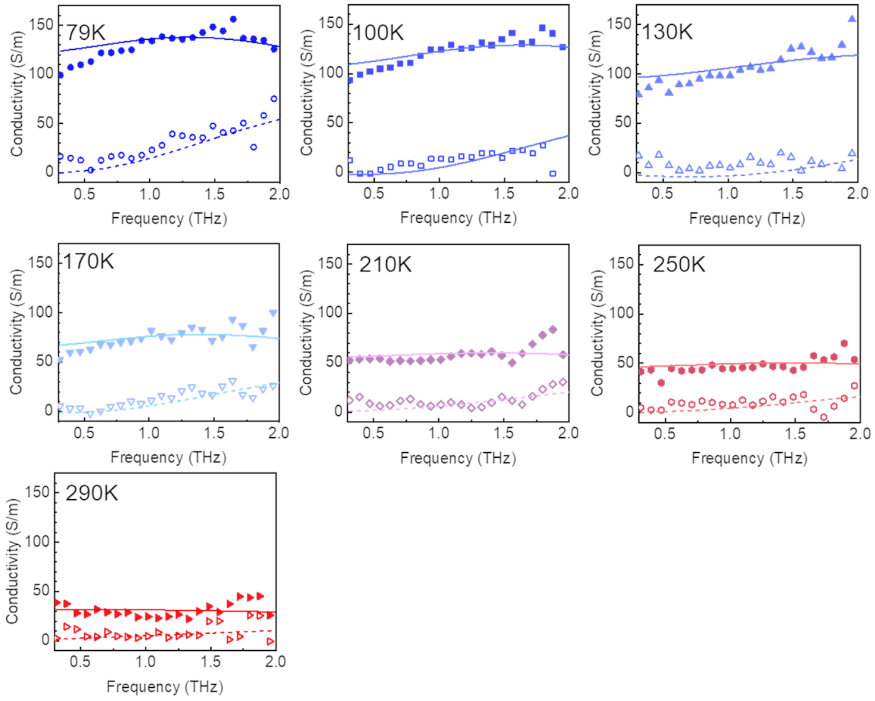

Figure 4.8: Frequency resolved photoconductivity data and relative Drude-Smith fit for the first sample of PA75-PANI. Full symbols represents the real part of the photoconductivity, while open ones represent the imaginary component.

For the sake of reproducibility, we measured a second sample that was synthesized and treated identically. The data are reported in Figure 4.9.

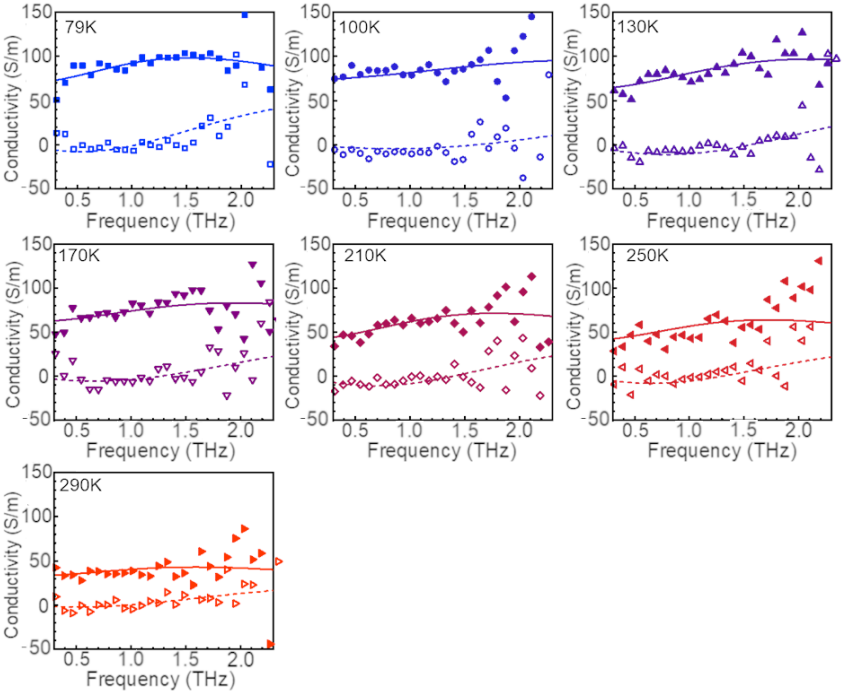

Figure 4.9: Frequency resolved photoconductivity data and relative Drude-Smith fit for the second sample of PA75-PANI. Full symbols represents the real part of the photoconductivity, while open ones represent the imaginary component.

Temperature dependence of optical absorption

Figure 4.10 shows that the small absorption change can only contribute to a 10% of the signal in terms of excitation probability increase and cannot justify the drastic decrease of ω_p alone, given that laser excitation was constant throughout the whole experiment. Therefore, we ascribe the decrease in ω_p to a reduction of the photon-to-charge conversion yield or to an increase in the particle effective mass. We hypothesize however that a decreasing yield with temperature is not consistent with the notion of thermally assisted charge separation and exciton dissociation. The

effective mass used to calculate the carrier density is considered equal to the electron mass.

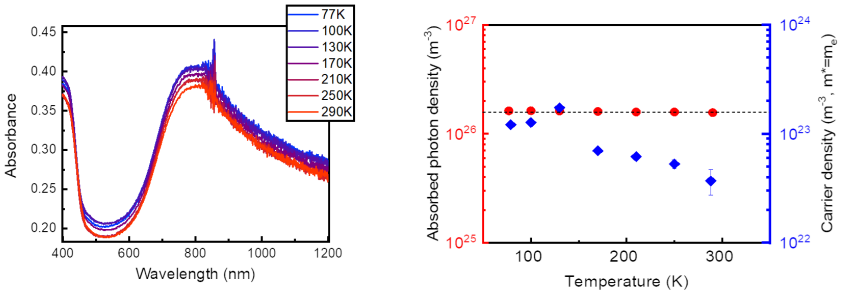

Figure 4.10: Absorbance of PA75-PANI as a function of temperature (left panel) and comparison between the absorbed photon density and the charge density extracted from ω_p of the Drude-Smith fit.

Alternative approach for temperature dependence

The following analysis was freely inspired by the work of Li *et al.* (2014).[96] The idea is to overcome the difficulties of the interpretation of the parameters that appear in the Drude-Smith formulation mentioned earlier in Section 1.1.2. We start with a definition of effective mass m^*, obtained from the integral of the real part of the Drude Equation (1.11), evaluated over the angular frequency ω.

$$\frac{1}{m^*} = \frac{2}{\pi n_0 e^2} \int_0^\infty \sigma(\omega) d\omega \tag{4.1}$$

With this inversion we have the advantage that we do not explicitly use the Drude-Smith parameters, avoiding misleading interpretations. In other words, the formula is used phenomenologically and empirically, only to return the shape that best explains the data. On the other side, the definition of optical mass in Equation (4.1) is valid only within the boundaries of the Drude model. We stretch the application to the Drude-

Smith case, with the assumption that is not so different from the pure Drude case. The extended fitting functions are reported in Figure 4.11.

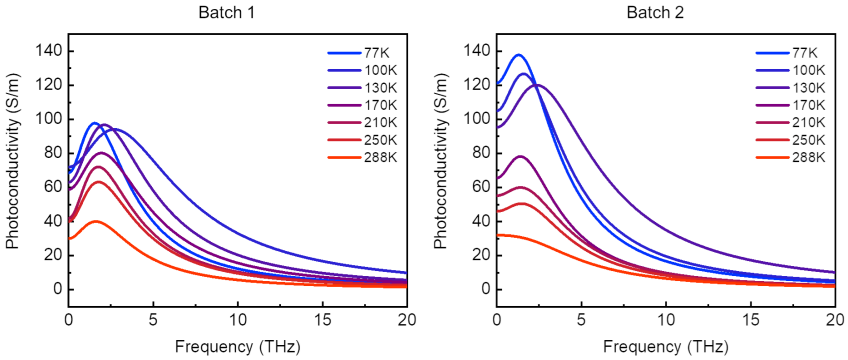

Figure 4.11: Drude-Smith fitting functions of the data showed in Figures 4.8 and 4.9. The plot is extrapolated until 20 THz for the evaluation of the integral in (4.1).

We introduced an arbitrary cut-off at 20 THz to the integral in Equation (4.1). With this operation, we are able to provide an estimate of the effective mass relative to the value assumed at room temperature (Figure 4.12).

Notably, we are able to qualitatively reproduce the photoconductivity data but we lack a valid estimate of the charge generation quantum yield to finally provide a quantitative comparison.

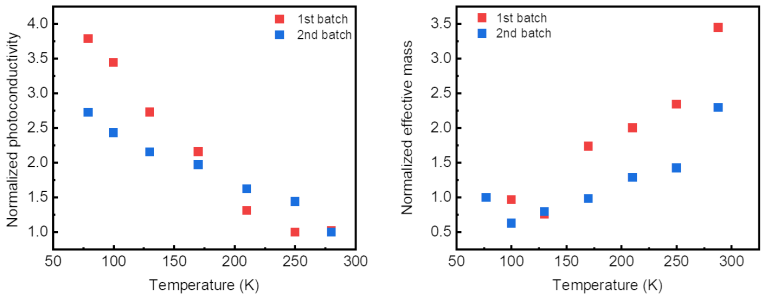

Figure 4.12: Comparison between the normalized photoconductivity at 15 ps after the photoexcitation (left panel) and the normalized effective mass calculated with the illustrated method (right panel).

Summary

emiconductors are undisputedly the class of materials that has driven the progress in electronics since the second half of the 20th century. As such, tools that can reliably assess their electric properties are of primary relevance for developing new technologies. Among these methods, in this thesis, we exploited time-resolved THz spectroscopy (TRTS) to study conductivity in semiconductors.

In the introductory chapter of this thesis, we presented an overview of the mechanism of electrical conductivity and the principal models to explain the phenomenon. Then, we focused our attention on the specific case of semiconductors, which we divided into two categories based on their chemistry: inorganic and carbon-based organic materials. For each class, we discussed the physical origin of the semiconducting behavior, based either on the nearly free electron or the tight-binding formalism. This represents the base from which we developed the discussion about the inorganic Copper-Indium, Gallium Selenide (CIGS), and organic polyaniline (PANI), the two materials that are the main object of the thesis.

The second chapter includes the description of the leading experimental methods adopted for the development of this thesis, *i.e.* TRTS. THz radiation's low photon energy makes it possible to probe systems where the separation between energy levels is relatively small, such as within energy bands in semiconductors or excitonic systems. In a typical experiment, an above gap excitation generates free carriers in the samples, that are monitored as a function of pump-probe delay with a freely propagating, single-cycle pulse in a 2 THz wide observable range. Measuring pump-

induced transmission changes of the complete THz waveform in the time domain also allows retrieving the complex-valued conductivity spectrum, from which transport figures of merit can be obtained unambiguously in a contactless fashion. In this respect, TRTS provide a powerful mean to scrutinize both time evolution of carrier population and charge transport mechanisms in semiconductors, both aspects are critical for optoelectronic devices.

In the third chapter, we studied TRTS carrier dynamics at the interface between CIGS and CdS, a heterojunction interface that is relevant for low-cost, thin-film photovoltaics. The width of the energy gap of CIGS alloys can be continuously tuned by Ga content, with the idea to reach the Shockley-Queisser efficiency limit. However, contrary to the expectations, better theoretical efficiency predicted in high bandgap CIGS-based devices turns into overall lower device performances when compared with low-gap devices. We demonstrated that the origin of this effect is linked to surface recombination at the CIGS/CdS interface. Recombination at this interface is drastically dependent on the CIGS energy gap and becomes dominant after a certain Ga content threshold.

In the last part of this thesis, we analyzed organic semiconductors. We presented an analysis of the conductivity in PANI thin films doped with a novel dopant: phytic acid. This new combination between a state-of-art polymer semiconductor and a new dopant reveals clear and distinct signatures of band-like transport. Drude responses in the THz window are obtained independent of doping content and, notably, independent of the sample's crystallinity. The latter is found to be decreased by doping content. Furthermore, temperature-dependent THz measurements reveal a monotone increase of charge mobility with decreasing temperature; scattering rates, though, are found to be almost invariant with temperature, so that the improvement in mobility is linked to either reduced effective mass or an improved photogeneration yield. These findings are singular among organic semiconductors and open the path for exploiting phytic acid as a novel, robust dopant in optoelectronic applications.

Samenvatting

Halfgeleiders zijn onbetwist dè materialen die de vooruitgang in de elektronica sinds de tweede helft van de 20e eeuw hebben aangedreven. Als zodanig zijn instrumenten die hun elektrische eigenschappen betrouwbaar kunnen bepalen van evident belang voor de ontwikkeling van nieuwe technologieën. In dit proefschrift hebben we gebruik gemaakt van tijdsopgeloste THz spectroscopie (TRTS) om de geleidbaarheid in halfgeleiders te bestuderen.

In het inleidende hoofdstuk van dit proefschrift hebben we een overzicht gegeven van het mechanisme van elektrische geleiding in het algemeen, alsook de belangrijkste modellen om dit fenomeen te verklaren. Daarna hebben we onze aandacht gericht op het specifieke geval van halfgeleiders. Halfgeleiders kunnen worden onderverdeeld in twee categorieën op basis van hun chemie: anorganische en op koolstof gebaseerde, organische materialen. Voor elke klasse bespraken wij de fysische oorsprong van het halfgeleidende gedrag, gebaseerd op hetzij het bijna-vrije elektron, hetzij het tight-binding formalisme. Dit vormt de basis voor de discussie over het anorganische koper-indium-galium-selenide (CIGS) en het organische polyaniline (PANI), de twee halfgeleidende materialen die het hoofdonderwerp van dit proefschrift vormen.

Het tweede hoofdstuk bevat de beschrijving van de belangrijkste experimentele methoden die voor de ontwikkeling van dit proefschrift zijn gebruikt, nl. TRTS. Dankzij de lage fotonenergie van THz straling is het mogelijk om systemen te onderzoeken waar de scheiding tussen energieniveaus relatief klein is, zoals binnen energiebanden in halfgeleiders of in excitonische systemen. In een typisch experiment genereert excitatie met

een foton energie hoger dan de bandgap van de halfgeleider vrije dragers in de halfgeleider. Die vrije ladingsdragers worden gevolgd in de tijd m.b.v. van een detectie (probe) puls: een laser puls met slechts één cyclus van het electromagnetisch veld. Die puls heeft een bandbreedte (1 THz) in het frequentiedomein die vergelijkbaar is met de 1 THz dragerfrequentie. Het meten van pomp-geïnduceerde transmissieveranderingen van de volledige THz golfvorm in het tijdsdomein maakt het ook mogelijk om de reële en imaginaire componenten van het complexe geleidbaarheidsspectrum te bepalen. Hieruit kunnen ondubbelzinnig transportparameters worden verkregen, op een contactloze manier. In dit opzicht is TRTS een uitstekende techniek om zowel de tijdsevolutie van de dragerpopulatie als de ladingsvervoersmechanismen in halfgeleiders te onderzoeken. Beide aspecten zijn kritisch voor opto-elektronische apparaten.

In het derde hoofdstuk bestudeerden we TRTS ladingsdragerdynamica op het grensvlak tussen CIGS en CdS, een heterojunctie-grensvlak dat relevant is voor goedkope, dunne-film fotovoltaïsche systemen. De breedte van de bandgap van CIGS-legeringen kan continu worden afgestemd door het Ga-gehalte, met het idee om de Shockley-Queisser rendementslimiet te bereiken. Echter, in tegenstelling tot de verwachtingen, wordt het theoretisch hogere rendement voorspeld in CIGS-gebaseerde apparaten met een hoge bandgap in het algemeen niet behaald: de prestaties zijn typisch lagere in vergelijking met apparaten met een lage bandgap. Wij hebben aangetoond dat de oorsprong van dit effect verband houdt met oppervlakterecombinatie op het CIGS/CdS grensvlak. Recombinatie aan dit grensvlak is drastisch afhankelijk van de CIGS-bandgap en wordt dominant boven een bepaald Ga-drempelgehalte.

In het laatste deel van dit proefschrift hebben wij organische halfgeleiders geanalyseerd. We presenteerden een analyse van het geleidingsvermogen in PANI dunne films gedoteerd met een nieuwe doteringsstof: fytinezuur. Deze nieuwe combinatie tussen een state-of-the-art polymeer halfgeleider en een nieuw doteringsmiddel onthult duidelijke en duidelijke signaturen van band-achtig transport. Drude reacties in het THz venster

worden verkregen onafhankelijk van het doperingsgehalte en, in het bijzonder, onafhankelijk van de kristalliniteit van het sample. Deze laatste blijkt te verminderen met het doperingsgehalte. Bovendien onthullen temperatuurafhankelijke THz-metingen een monotone toename van de ladingsmobiliteit bij dalende temperatuur; de verstrooiingstijden blijken echter bijna onveranderlijk te zijn met de temperatuur, zodat de verbetering van de mobiliteit verband moet houden met ofwel een gerduceerde effectieve massa, ofwel een verhoogd fotogeneratie-rendement. Deze bevindingen zijn uniek voor organische halfgeleiders en openen de weg voor de exploitatie van fytinezuur als een nieuwe, robuuste doteringsstof in opto-elektronische toepassingen.

Bibliography

[1] G. Busch. *Early history of the physics and chemistry of semiconductors-from doubts to fact in a hundred years. European Journal of Physics*, vol. 10 4, pp. 254–264, **1989**.

[2] P. Drude. *Zur Elektronentheorie der Metalle. Annalen der Physik*, vol. 306 3, pp. 566–613, **1900**.

[3] A. Sommerfeld. *Zur Elektronentheorie der Metalle auf Grund der Fermischen Statistik - I. Teil: Allgemeines, Strömungs- und Austrittsvorgänge. Zeitschrift für Physik*, vol. 47 1-2, pp. 1–32, **1928**.

[4] N. Smith. *Drude theory and the optical properties of liquid mercury. Physics Letters A*, vol. 26 3, pp. 126–127, **1968**.

[5] T. L. Cocker, D. Baillie, M. Buruma, L. V. Titova, R. D. Sydora, F. Marsiglio, and F. A. Hegmann. *Microscopic origin of the Drude-Smith model. Physical Review B*, vol. 96 20, p. 205439, **2017**.

[6] P. Kužel and H. Němec. *Terahertz Spectroscopy of Nanomaterials: a Close Look at Charge-Carrier Transport*, **2020**.

[7] N. W. Ashcroft and N. D. Mermin. *Solid State Physics*. Saunders College Publishing, **1976**.

[8] C. Fritts. *On a new form of Selenium Photocell. American Journal of Physics*, vol. 3 26, pp. 465–472, **1883**.

[9] W. G. A. Day and R. E. *On the action of light on Selenium*, **1876**.

[10] M. S. Chowdhury, K. S. Rahman, T. Chowdhury, N. Nuthammachot, K. Techato, M. Akhtaruzzaman, S. K. Tiong, K. Sopian, and N. Amin. *An overview of solar photovoltaic panels' end-of-life material recycling*, **2020**.

[11] W. Shockley and H. J. Queisser. *Detailed Balance Limit of Efficiency of p-n Junction Solar Cells. Journal of Applied Physics*, vol. 32 3, p. 510, **1961**.

[12] National Renewable Energy Laboratory. *Solar Spectra | Grid Modernization | NREL*. https://www.nrel.gov/grid/solar-resource/spectra.html.

[13] T. D. Lee and A. U. Ebong. *A review of thin film solar cell technologies and challenges*, **2017**.

[14] J. Ramanujam and U. P. Singh. *Copper indium gallium selenide based solar cells - A review. Energy and Environmental Science*, vol. 10 6, pp. 1306–1319, **2017**.

[15] M. A. Green, E. D. Dunlop, J. Hohl-Ebinger, M. Yoshita, N. Kopidakis, and A. W. Ho-Baillie. *Solar cell efficiency tables (Version 55). Progress in Photovoltaics: Research and Applications*, vol. 28 1, pp. 3–15, **2020**.

[16] S. Binetti, P. Garattini, R. Mereu, A. Le Donne, S. Marchionna, A. Gasparotto, M. Meschia, I. Pinus, and M. Acciarri. *Fabricating Cu(In,Ga)Se2 solar cells on flexible substrates by a new roll-to-roll deposition system suitable for industrial applications. Semiconductor Science and Technology*, vol. 30 10, p. 105006, **2015**.

[17] S. Marchionna, P. Garattini, A. Le Donne, M. Acciarri, S. Tombolato, and S. Binetti. *Cu2ZnSnS4 solar cells grown by sulphurisation of sputtered metal precursors. Thin Solid Films*, vol. 542, pp. 114–118, **2013**.

[18] C. Marchi, &. G. Panzeri, &. L. Pedrazzetti, M. I. Khalil, &. A. Lucotti, &. J. Parravicini, &. M. Acciarri, &. S. Binetti, and &. L. Magagnin. *One-step CZT electroplating from alkaline solution on flexible Mo foil for CZTS absorber. Journal of Solid State Electrochemistry*, **2021**.

[19] C. K. Chiang, C. R. Fincher, Y. W. Park, A. J. Heeger, H. Shirakawa, E. J. Louis, S. C. Gau, and A. G. MacDiarmid. *Electrical conductivity in doped polyacetylene. Physical Review Letters*, vol. 39 17, pp. 1098–1101, **1977**.

[20] A. J. Heeger, S. Kivelson, J. R. Schrieffer, and W. P. Su. *Solitons in conducting polymers. Reviews of Modern Physics*, vol. 60 3, pp. 781–850, **1988**.

[21] T. Odajima, M. Ashizawa, Y. Konosu, H. Matsumoto, and T. Mori. *The impact of molecular planarity on electronic devices in thienoisoindigo-based organic semiconductors. Journal of Materials Chemistry C*, vol. 2 48, pp. 10455–10467, **2014**.

[22] H. Fröhlich. *On the theory of superconductivity: the one-dimensional case. Proceedings of the Royal Society of London. Series A. Mathematical and Physical Sciences*, vol. 223 1154, pp. 296–305, **1954**.

[23] J. P. Pouget. *The Peierls instability and charge density wave in one-dimensional electronic conductors. Comptes Rendus Physique*, vol. 17 3-4, pp. 332–356, **2016**.

[24] J. L. Bredas and G. B. Street. *Polarons, Bipolarons, and Solitons in Conducting Polymers. Accounts of Chemical Research*, vol. 18 10, pp. 309–315, **1985**.

[25] H. Méndez, G. Heimel, A. Opitz, K. Sauer, P. Barkowski, M. Oehzelt, J. Soeda, T. Okamoto, J. Takeya, J.-B. Arlin, J.-Y. Balandier, Y. Geerts, N. Koch, and I. Salzmann. *Doping of Organic Semiconductors: Impact of Dopant Strength and Electronic Coupling. Angewandte Chemie International Edition*, vol. 52 30, pp. 7751–7755, **2013**.

[26] I. E. Jacobs and A. J. Moulé. *Controlling Molecular Doping in Organic Semiconductors. Advanced Materials*, vol. 29 42, p. 1703063, **2017**.

[27] J. H. Bombile, M. J. Janik, and S. T. Milner. *Polaron formation mechanisms in conjugated polymers. Physical Chemistry Chemical Physics*, vol. 20 1, pp. 317–331, **2017**.

[28] R. P. McCall, J. M. Ginder, J. M. Leng, H. J. Ye, S. K. Manohar, J. G. Masters, G. E. Asturias, A. G. MacDiarmid, and A. J. Epstein. *Spectroscopy and defect states in polyaniline. Physical Review B*, vol. 41 8, pp. 5202–5213, **1990**.

[29] J. C. Chiang and A. G. MacDiarmid. *'Polyaniline': Protonic acid doping of the emeraldine form to the metallic regime. Synthetic Metals*, vol. 13 1-3, pp. 193–205, **1986**.

[30] X. C. Zhang, Y. Jin, and X. F. Ma. *Coherent measurement of THz optical rectification from electro-optic crystals. Applied Physics Letters*, vol. 61 23, pp. 2764–2766, **1992**.

[31] A. Nahata, D. H. Auston, T. F. Heinz, and C. Wu. *Coherent detection of freely propagating terahertz radiation by electro-optic sampling. Applied Physics Letters*, vol. 68 2, pp. 150–152, **1996**.

[32] C. Winnewisser, P. Uhd Jepsen, M. Schall, V. Schyja, and H. Helm. *Electro-optic detection of THz radiation in LiTaO3, LiNbO3 and ZnTe. Applied Physics Letters*, vol. 70 23, pp. 3069–3071, **1997**.

[33] R. Ulbricht, E. Hendry, J. Shan, T. F. Heinz, and M. Bonn. *Carrier dynamics in semiconductors studied with time-resolved terahertz spectroscopy. Reviews of Modern Physics*, vol. 83 2, pp. 543–586, **2011**.

[34] C. a. Schmuttenmaer. *Exploring dynamics in the far infrared with terahertz spectroscopy. Chem. Rev.*, vol. 104, pp. 1759–1780, **2004**.

[35] J. T. Kindt. *Theory for determination of the low-frequency time-dependent response function in liquids using time-resolved terahertz*

pulse spectroscopy. Journal of Chemical Physics, vol. 110 17, pp. 8589–8596, **1999**.

[36] H. Němec, F. Kadlec, and P. Kužel. *Methodology of an optical pump-terahertz probe experiment: An analytical frequency-domain approach. Journal of Chemical Physics*, vol. 117 18, pp. 8454–8465, **2002**.

[37] P. Kužel, F. Kadlec, and H. Němec. *Propagation of terahertz pulses in photoexcited media: Analytical theory for layered systems. Journal of Chemical Physics*, vol. 127 2, p. 024506, **2007**.

[38] P. D. Cunningham. *Accessing terahertz complex conductivity dynamics in the time-domain. IEEE Transactions on Terahertz Science and Technology*, vol. 3 4, pp. 494–498, **2013**.

[39] M. A. Green, E. D. Dunlop, D. H. Levi, J. Hohl-Ebinger, M. Yoshita, A. W. Ho-Baillie, Y. Hishikawa, E. D. Dunlop, D. H. Levi, J. Hohl-Ebinger, M. Yoshita, and A. W. Ho-Baillie. *Solar cell efficiency tables (Version 54). Progress in Photovoltaics: Research and Applications*, vol. 27, **2019**.

[40] A. Chirilă, S. Buecheler, F. Pianezzi, P. Bloesch, C. Gretener, A. R. Uhl, C. Fella, L. Kranz, J. Perrenoud, S. Seyrling, R. Verma, S. Nishiwaki, Y. E. Romanyuk, G. Bilger, and A. N. Tiwari. *Highly efficient Cu(In,Ga)Se2 solar cells grown on flexible polymer films. Nature Materials*, vol. 10 11, pp. 857–861, **2011**.

[41] J. F. Guillemoles, L. Kronik, D. Cahen, U. Rau, A. Jasenek, and H. W. Schock. *Stability Issues of Cu(In,Ga)Se2-Based Solar Cells. Journal of Physical Chemistry B*, vol. 104 20, pp. 4849–4862, **2000**.

[42] S. Rühle. *Tabulated values of the Shockley-Queisser limit for single junction solar cells. Solar Energy*, vol. 130, pp. 139–147, **2016**.

[43] R. Herberholz, V. Nadenau, U. Rühle, C. Köble, H. Schock, and B. Dimmler. *Prospects of wide-gap chalcopyrites for thin film photo-*

voltaic modules. Solar Energy Materials and Solar Cells, vol. 49 1-4, pp. 227–237, **1997**.

[44] W. N. Shafarman, R. Klenk, and B. E. Mccandless. *Device and material characterization of Cu(InGa)Se 2 solar cells with increasing band gap. Journal of Applied Physics*, vol. 79, p. 7324, **1996**.

[45] A. Yamada, K. Matsubara, K. Sakurai, S. Ishizuka, H. Tampo, P. J. Fons, K. Iwata, and S. Niki. *Effect of band offset on the open circuit voltage of heterojunction CuIn1-xGaxSe2 solar cells. Applied Physics Letters*, vol. 85 23, pp. 5607–5609, **2004**.

[46] P. K. Nayak, S. Mahesh, H. J. Snaith, and D. Cahen. *Photovoltaic solar cell technologies: analysing the state of the art. Nature Reviews Materials*, vol. 4 4, pp. 269–285, **2019**.

[47] Y.-J. Zhao, C. Persson, S. Lany, and A. Zunger. *Why can CuInSe2 be readily equilibrium-doped n-type but the wider-gap CuGaSe2 cannot? Applied Physics Letters*, vol. 85 24, pp. 5860–5862, **2004**.

[48] S. Zhang, S. H. Wei, A. Zunger, and H. Katayama-Yoshida. *Defect physics of the chalcopyrite semiconductor. Physical Review B - Condensed Matter and Materials Physics*, vol. 57 16, pp. 9642–9656, **1998**.

[49] G. Hanna, A. Jasenek, U. Rau, and H. Schock. *Influence of the Ga-content on the bulk defect densities of Cu(In,Ga)Se2. Thin Solid Films*, vol. 387 1-2, pp. 71–73, **2001**.

[50] J. T. Heath, J. D. Cohen, W. N. Shafarman, D. X. Liao, and A. A. Rockett. *Effect of Ga content on defect states in CuIn 1-x Ga x Se 2 photovoltaic devices. Appl. Phys. Lett*, vol. 80, p. 4540, **2002**.

[51] S. Shirakata, K. Ohkubo, Y. Ishii, and T. Nakada. *Effects of CdS buffer layers on photoluminescence properties of Cu(In,Ga)Se2 solar cells. Solar Energy Materials and Solar Cells*, vol. 93 6, pp. 988–992, **2009**.

[52] S. Lany and A. Zunger. *Light- and bias-induced metastabilities in Cu(In,Ga)Se2 based solar cells caused by the (VSe-VCu) vacancy complex. Journal of Applied Physics*, vol. 100 11, p. 113725, **2006**.

[53] L. Kronik, D. Cahen, and H. W. Schock. *Effects of Sodium on Polycrystalline Cu(In,Ga)Se2 and Its Solar Cell Performance. Advanced Materials*, vol. 10 1, pp. 31–36, **1998**.

[54] D. W. Niles, M. Al-Jassim, and K. Ramanathan. *Direct observation of Na and O impurities at grain surfaces of CuInSe2 thin films. Journal of Vacuum Science & Technology A: Vacuum, Surfaces, and Films*, vol. 17 1, pp. 291–296, **1999**.

[55] T. Minemoto, T. Matsui, H. Takakura, Y. Hamakawa, T. Negami, Y. Hashimoto, T. Uenoyama, and M. Kitagawa. *Theoretical analysis of the effect of conduction band offset of window/CIS layers on performance of CIS solar cells using device simulation. Solar Energy Materials and Solar Cells*, vol. 67 1, pp. 83–88, **2001**.

[56] R. Klenk. *Characterisation and modelling of chalcopyrite solar cells. Thin Solid Films*, vol. 387 1-2, pp. 135–140, **2001**.

[57] F. Couzinié-Devy, N. Barreau, and J. Kessler. *Re-investigation of preferential orientation of Cu(In,Ga)Se2 thin films grown by the three-stage process. Progress in Photovoltaics: Research and Applications*, vol. 19 5, pp. 527–536, **2011**.

[58] H. Němec, P. Ǩuel, and V. Sundström. *Charge transport in nanostructured materials for solar energy conversion studied by time-resolved terahertz spectroscopy. Journal of Photochemistry and Photobiology A: Chemistry*, vol. 215 2-3, pp. 123–139, **2010**.

[59] P. Kužel, F. Kadlec, and H. Němec. *Propagation of terahertz pulses in photoexcited media: Analytical theory for layered systems. J. Chem. Phys*, vol. 127, p. 24506, **2007**.

[60] P. Jepsen, D. Cooke, and M. Koch. *Terahertz spectroscopy and imaging - Modern techniques and applications. Laser & Photonics Reviews*, vol. 5 1, pp. 124–166, **2011**.

[61] P. D. Paulson, R. W. Birkmire, and W. N. Shafarman. *Optical characterization of CuIn1-xGaxSe2 alloy thin films by spectroscopic ellipsometry. Journal of Applied Physics*, vol. 94 2, pp. 879–888, **2003**.

[62] R. Chen and C. Persson. *Parameterization of CuIn1-xGaxSe2 (x = 0, 0.5, and 1) energy bands. Thin Solid Films*, vol. 519, pp. 7503–7507. Elsevier, **2011**.

[63] M. Lambsdorff, J. Kuhl, J. Rosenzweig, A. Axmann, and J. Schneider. *Subpicosecond carrier lifetimes in radiation-damaged GaAs. Applied Physics Letters*, vol. 58 17, pp. 1881–1883, **1991**.

[64] H. Wang, I. Barceló, T. Lana-Villarreal, R. Gómez, M. Bonn, and E. Cánovas. *Interplay between structure, stoichiometry, and electron transfer dynamics in SILAR-based quantum dot-sensitized oxides. Nano Letters*, vol. 14 10, pp. 5780–5786, **2014**.

[65] F. E. Doany, D. Grischkowsky, and C. Chi. *Carrier lifetime versus ion-implantation dose in silicon on sapphire. Applied Physics Letters*, vol. 50 8, pp. 460–462, **1987**.

[66] W. Jaegermann, A. Klein, and T. Mayer. *Interface Engineering of Inorganic Thin-Film Solar Cells - Materials-Science Challenges for Advanced Physical Concepts. Advanced Materials*, vol. 21 42, pp. 4196–4206, **2009**.

[67] M. Wan and J. Yang. *Mechanism of proton doping in polyaniline. Journal of Applied Polymer Science*, vol. 55 3, pp. 399–405, **1995**.

[68] E. S. Matveeva. *Could the acid doping of polyaniline represent the charge transfer interaction? Synthetic Metals*, vol. 83 2, pp. 89–96, **1996**.

[69] G. Zotti and G. Schiavon. *Spectroclectrochemical determination of polarons in polypyrrole and polyaniline. Synthetic Metals*, vol. 30 2, pp. 151–158, **1989**.

[70] A. J. Epstein, J. M. Ginder, F. Zuo, R. W. Bigelow, H. S. Woo, D. B. Tanner, A. F. Richter, W. S. Huang, and A. G. MacDiarmid. *Insulator-to-metal transition in polyaniline. Synthetic Metals*, vol. 18 1-3, pp. 303–309, **1987**.

[71] Z. H. Wang, E. M. Scherr, A. G. MacDiarmid, and A. J. Epstein. *Transport and EPR studies of polyaniline: A quasi-one-dimensional conductor with three-dimensional metallic states. Physical Review B*, vol. 45 8, pp. 4190–4202, **1992**.

[72] R. Noriega, J. Rivnay, K. Vandewal, F. P. V. Koch, N. Stingelin, P. Smith, M. F. Toney, and A. Salleo. *A general relationship between disorder, aggregation and charge transport in conjugated polymers. Nature Materials*, vol. 12 11, pp. 1038–1044, **2013**.

[73] K. Kang, S. Watanabe, K. Broch, A. Sepe, A. Brown, I. Nasrallah, M. Nikolka, Z. Fei, M. Heeney, D. Matsumoto, K. Marumoto, H. Tanaka, S. I. Kuroda, and H. Sirringhaus. *2D coherent charge transport in highly ordered conducting polymers doped by solid state diffusion. Nature Materials*, vol. 15 8, pp. 896–902, **2016**.

[74] I. Y. Choi, J. Lee, H. Ahn, J. Lee, H. C. Choi, and M. J. Park. *High-Conductivity Two-Dimensional Polyaniline Nanosheets Developed on Ice Surfaces. Angewandte Chemie - International Edition*, vol. 54 36, pp. 10497–10501, **2015**.

[75] H. Terrones, M. Terrones, E. Hernández, N. Grobert, J. C. Charlier, and P. M. Ajayan. *New metallic allotropes of planar and tubular carbon. Physical Review Letters*, vol. 84 8, pp. 1716–1719, **2000**.

[76] R. A. Street. *The benefit of order*, **2006**.

[77] K. Lee, S. Cho, H. P. Sung, A. J. Heeger, C. W. Lee, and S. H. Lee. *Metallic transport in polyaniline. Nature*, vol. 441 1, pp. 65–68, **2006**.

[78] T. Zhang, H. Qi, Z. Liao, Y. D. Horev, L. A. Panes-Ruiz, P. S. Petkov, Z. Zhang, R. Shivhare, P. Zhang, K. Liu, V. Bezugly, S. Liu, Z. Zheng, S. Mannsfeld, T. Heine, G. Cuniberti, H. Haick, E. Zschech, U. Kaiser, R. Dong, and X. Feng. *Engineering crystalline quasi-two-dimensional polyaniline thin film with enhanced electrical and chemiresistive sensing performances. Nature Communications*, vol. 10 1, p. 4225, **2019**.

[79] L. Pan, G. Yu, D. Zhai, H. R. Lee, W. Zhao, N. Liu, H. Wang, B. C.-K. Tee, Y. Shi, Y. Cui, and Z. Bao. *Hierarchical nanostructured conducting polymer hydrogel with high electrochemical activity. Proceedings of the National Academy of Sciences*, vol. 109 24, pp. 9287–9292, **2012**.

[80] D. Venkateshvaran, M. Nikolka, A. Sadhanala, V. Lemaur, M. Zelazny, M. Kepa, M. Hurhangee, A. J. Kronemeijer, V. Pecunia, I. Nasrallah, I. Romanov, K. Broch, I. McCulloch, D. Emin, Y. Olivier, J. Cornil, D. Beljonne, and H. Sirringhaus. *Approaching disorder-free transport in high-mobility conjugated polymers. Nature*, vol. 515 7527, pp. 384–388, **2014**.

[81] W. S. Huang and A. G. MacDiarmid. *Optical properties of polyaniline. Polymer*, vol. 34 9, pp. 1833–1845, **1993**.

[82] A. MacDiarmid and A. J. Epstein. *The concept of secondary doping as applied to polyaniline. Synthetic Metals*, vol. 65 2-3, pp. 103–116, **1994**.

[83] M. C. Beard, G. M. Turner, and C. A. Schmuttenmaer. *Terahertz Spectroscopy. Spectroscopy*, pp. 910–927, **2002**.

[84] E. Hendry, M. Koeberg, J. M. Schins, L. D. A. Siebbeles, and M. Bonn. *Free carrier photogeneration in polythiophene versus poly(phenylene vinylene) studied with THz spectroscopy. Chemical Physics Letters*, vol. 432 4-6, pp. 441–445, **2006**.

[85] Z. Jin, D. Gehrig, C. Dyer-Smith, E. J. Heilweil, F. Laquai, M. Bonn, and D. Turchinovich. *Ultrafast terahertz photoconductivity of photovoltaic polymer-fullerene blends: A comparative study correlated with photovoltaic device performance. Journal of Physical Chemistry Letters*, vol. 5 21, pp. 3662–3668, **2014**.

[86] F. A. Hegmann, R. R. Tykwinski, K. P. Lui, J. E. Bullock, and J. E. Anthony. *Picosecond Transient Photoconductivity in Functionalized Pentacene Molecular Crystals Probed by Terahertz Pulse Spectroscopy. Physical Review Letters*, vol. 89 22, p. 227403, **2002**.

[87] T. Unuma, N. Yamada, A. Nakamura, H. Kishida, S. C. Lee, E. Y. Hong, S. H. Lee, and O. P. Kwon. *Direct observation of carrier delocalization in highly conducting polyaniline. Applied Physics Letters*, vol. 103 5, p. 053303, **2013**.

[88] G. Kim, S. J. Kang, G. K. Dutta, Y. K. Han, T. J. Shin, Y. Y. Noh, and C. Yang. *A thienoisoindigo-naphthalene polymer with ultrahigh mobility of 14.4 cm2/V · s that substantially exceeds benchmark values for amorphous silicon semiconductors. Journal of the American Chemical Society*, vol. 136 26, pp. 9477–9483, **2014**.

[89] J. M. Ginder, A. J. Epstein, and A. G. MacDiarmid. *Ring-rotational defects in polyaniline. Solid State Communications*, vol. 72 10, pp. 987–990, **1989**.

[90] J. M. Ginder, A. J. Epstein, and A. G. Macdiarmid. *Ring-torsional polarons in polyaniline and polyparaphenylene sulfide. Synthetic Metals*, vol. 43 1-2, pp. 3431–3436, **1991**.

[91] R. P. McCall, M. G. Roe, J. M. Ginder, T. Kusumoto, A. J. Epstein, G. E. Asturias, E. M. Scherr, and A. G. MacDiarmid. *IR absorption, photoinduced IR absorption, and photoconductivity of polyaniline. Synthetic Metals*, vol. 29 1, pp. 433–438, **1989**.

[92] R. Patil, Y. Harima, K. Yamashita, K. Komaguchi, Y. Itagaki, and M. Shiotani. *Charge carriers in polyaniline film: A correlation between mobility and in-situ ESR measurements. Journal of Electroanalytical Chemistry*, vol. 518 1, pp. 13–19, **2002**.

[93] D. Emin. *Optical properties of large and small polarons and bipolarons. Physical Review B*, vol. 48 18, pp. 13691–13702, **1993**.

[94] V. Coropceanu, J. Cornil, D. A. da Silva Filho, Y. Olivier, R. Silbey, and J. L. Brédas. *Charge transport in organic semiconductors*, **2007**.

[95] D. Chattopadhyay and H. J. Queisser. *Electron scattering by ionized impurities in semiconductors. Reviews of Modern Physics*, vol. 53 4, pp. 745–768, **1981**.

[96] Y. Li, Y. Yi, V. Coropceanu, and J. L. Brédas. *Optical conductivity and optical effective mass in a high-mobility organic semiconductor: Implications for the nature of charge transport. Physical Review B - Condensed Matter and Materials Physics*, vol. 90 24, p. 245112, **2014**.

[97] X. Wang and A. Dodabalapur. *Going beyond polaronic theories in describing charge transport in rubrene single crystals. Applied Physics Letters*, vol. 116 9, p. 093301, **2020**.

Acknowledgements

The preparation of this thesis represents the conclusion of a chapter of my life and it could not be possible without all the people that supported me that in many different ways. These last few lines are dedicated to them.

At first, I would start to share my gratitude to my supervisor Mischa Bonn, for the opportunity he offered and the guidance over the course of my staying in the Molecular Spectroscopy department. Then, the next huge thank is for Enrique Cànovas, who accompanied me in each step of the doctorate from the very beginning. Even after you moved to Spain, you were still able to be present, supporting, inspirational and motivating.

I would like to continue to thank my mentors at the University of Milano-Bicocca Francesco Meinardi, Angelo Monguzzi and Sergio Brovelli for teaching me what is like to be a scientist and for having introduced me to this career.

Even though he cannot read this dedication anymore, the period of my life that just passed would have not been the same without Eduard Unger. I loved to share with you all the challenges, the problems, the most crazy ideas and all the funny happenings of the MPI, but most importantly, your friendship outside the institute had a deep influence on me. It is unfortunate that it did not have the chance to continue.

Of course I cannot forget the last member of the original office 1.408 trio Yu-Jen. I am already missing our discussions always ending up talking about dining, but I have to say that I am not missing at all your baseball practice at a palm distance with me chilling on the sofa. I have still nightmares. I wish you all the best for your highest goals, even if I already

know that, at the very least, you will be successful. Naturally, expect me to appear in Taiwan from time to time.

I won't forget the rest of the people that spend some time in the same beautiful office: Kevin, Yelena, Veronica, Martin, Sven. You all contributed to the daily dose of happiness. I would also like to thank all the rest of the members of AK-Bonn, and in particular the THz people for all the help, the scientific support and the always fruitful discussions: Hai, Maksim, Hassan, Keno, Ivan, Wentao, Alex, Xiaoyu, Paniz, Heng, Shuai, Wenhao, Xiaoqing and Simon.

To the real soul of the department: Laurie. Thank you for all the nice talks and the help in all the moments I was disoriented in the maze of German bureaucracy, which means continuously from the day I started until now.

Going onwards, living in Mainz wouldn't have been bearable without the sprinkle of some Mediterranean vibes here and there. For this, I have to thank Dimitra, Alexandra and Stela. I loved the talks we had together and they are for sure one of the things I will miss the most from Mainz. A huge thank also to the members of the Italian crew Alessia, Claudio, Giovanni, Roberto, Gabriele and to the newer additions Alessandro e Lucia.

A special mention to the Kendo group of the USC Mainz. I joined the dojo almost by accident and I was immediately caught in a spiral of athleticism, fun, but also meditation, which was able to reset my mind during every training session. It wouldn't be possible without the charisma and passion of Frank, Tino and Carsten sensei, Rute and my fellow kenshi Alexey, Moritz, Stavros, Aurelio, Stephan and Alex.

Now I must thank the lovely Große Bleiche WG: Alex, Nikolina, Henrik and Desiree. Living together during difficult times such as the recent pandemic, turned to be the perfect occasion to meet wonderful people.

After the German adventure, I finally migrated south and I received a great welcome as soon as I landed in Spain. For this I am grateful to Vasilis, Natalia, Sergio, Miguel Angel, Victor, Saül, Luis and Jorge.

To all my friends in Italy: Bura, Cami, Cuc, Digio, Gio, Lele, Mari, Mero, Taglia. It is fantastic to count on a solid, everlasting friendship started between school's desks. Every time I come back home, it is important that "it feels like I have never left".

To the Mellon, so scattered around the world yet always connected by a deep bond that periodically brings us close again.

The most important note goes to my 'little' brother Andrea, who maybe unconsciously is always motivating and able to put a smile on my face.

Cara mamma, caro papà, cara nonna, zii, zie e cugini, vi ho lasciato in fondo a questa pagina, ma certamente non significa che siete meno importanti. Grazie di tutto il sostegno e l'affetto che mi date ogni giorno.